NATURAL MELANIN NANOPARTICLES FOR PHOTOTHERMAL THERAPY: A COMPARATIVE STUDY OF METAL ION-CHELATED AND NON-CHELATED FORMS

by

Melike Demirtaş

B.S., in Biomedical Engineering, Pamukkale University, 2020

Submitted to the Institute of Biomedical Engineering
in partial fulfillment of the requirements
for the degree of
Master of Science
in
Biomedical Engineering

Boğaziçi University
2025

NATURAL MELANIN NANOPARTICLES FOR PHOTOTHERMAL THERAPY: A COMPARATIVE STUDY OF METAL ION-CHELATED AND NON-CHELATED FORMS

APPROVED BY:

Assist. Prof. Dr. Mustafa Kemal Ruhi .....
(Thesis Advisor)

Assist. Prof. Dr. Engin Baysoy .....
(Thesis Co-advisor)

Assist. Prof. Dr. Gizem Kaleli Can .....

Assist. Prof. Dr. Canan Bağcı .....

Assist. Prof. Dr. Pınar S. Özbay .....

DATE OF APPROVAL: 30 June 2025

ACKNOWLEDGMENTS

I would like to thank to my advisor, Mustafa Kemal Ruhi and my co-advisor, Engin Baysoy, for guiding me through this research, teaching me how to navigate uncertainty until clarity emerged, and patiently answering my endless questions. Your critical insights and guidance have been more valuable to me than anything I could find in a book.

I am grateful to dear lab mates, Ayşe, Tuğçe and Oğuz, who made even the most difficult experiments bearable and even fun. Their mentorship and our collaborative brainstorming sessions made this journey an incredibly enjoyable experience.

My deepest gratitude should go to my family, whose unwavering support, endless encouragement, and unconditional love were always with me.

Moreover, this work received funding from the Boğaziçi University Research Fund under grant number 20333.

ACADEMIC ETHICS AND INTEGRITY STATEMENT

I, Melike Demirtaş, hereby certify that I am aware of the Academic Ethics and Integrity Policy issued by the Council of Higher Education (YÖK) and I fully acknowledge all the consequences due to its violation by plagiarism or any other way.

Name :

Signature:

Date:

ABSTRACT

NATURAL MELANIN NANOPARTICLES FOR PHOTOTHERMAL THERAPY: A COMPARATIVE STUDY OF METAL ION-CHELATED AND NON-CHELATED FORMS

Melanin nanoparticles (MNPs) chelated with metal ions have attracted increasing interest for theranostic applications. However, the effect of metal ion chelation on the photothermal therapy (PTT) performance of MNPs remains largely unexplored. This study investigates the PTT potential of melanin-based nanoparticles (MBNPs), focusing on the effects of irradiation wavelength and iron chelation. MNPs and Fe^{3+}-chelated melanin nanoparticles (MNP-Fe^{3+}) were synthesized and applied to prostate cancer cells. First, a cytotoxicity assay was performed to identify the highest non-toxic concentrations of the nanoparticles. Fe^{3+}-chelated MNPs showed reduced cytotoxicity, indicating that melanin may mitigate the toxic effects of Fe^{3+} ions, which is an advantageous property for their use as contrast agents in magnetic resonance imaging (MRI). Given the broad absorption spectrum of MBNPs spanning 200-800 nm, three distinct wavelengths (530 nm, 660 nm, and 785 nm) were selected to use in PTT experiments. Among the tested wavelengths, only irradiation at 785 nm led to significant reduction in cell viability. For non-chelated MNPs, cell survival decreased to approximately 50% in the 20 min PTT group. For the MNP-Fe^{3+}, the survival was reduced to around 40% in the 10 min PTT and further declined to about 30% following 20 min PTT treatment. Live/dead staining was performed solely for the 785 nm group, confirming the cell death patterns observed in the MTT assay. Therefore, our results showed that Fe^{3+} chelation enhanced the photothermal activity of MNPs. These findings suggest that Fe^{3+} chelation of MNPs, already known to enhance MRI contrast, also improves their biocompatibility and PTT efficacy.

Keywords: Melanin Nanoparticles, Fe^{3+}-chelated Melanin Nanoparticles, Photothermal Therapy

ÖZET

FOTOTERMAL TERAPİ İÇİN DOĞAL MELANİN NANOPARTİKÜLLERİ: METAL İYONU ŞELATLI VE ŞELATSIZ FORMLARIN KARŞILAŞTIRMALI BİR ÇALIŞMASI

Metal iyonlarıyla şelatlanmış melanin nanopartikülleri (MNP'ler) teranostik uygulamalar için giderek artan bir ilgi görmektedir. Fakat, metal iyon şelatlanmasının MNP'lerin fototermal terapi (PTT) performansı üzerindeki etkisi büyük ölçüde incelenmemiş durumdadır. Bu çalışma, ışınlama dalga boyu ve demir şelatlanması etkilerine odaklanarak melanin bazlı nanopartiküllerin (MBNP'ler) PTT potansiyelini araştırmaktadır. MNP'ler ve Fe^{3+}-şelatlanmış melanin nanopartikülleri (MNP-Fe^{3+}) sentezlendi ve prostat kanseri hücrelerine uygulandı. Nanopartiküllerin en yüksek toksik olmayan konsantrasyonlarını belirlemek için sitotoksisite testi yapıldı. Fe^{3+}-şelatlanmış MNP'ler azaltılmış sitotoksisite gösterdi ve bu, melaninin Fe^{3+} iyonlarının toksik etkilerini hafifletebileceğini ve manyetik rezonans görüntülemede (MRI'da) kontrast madde olarak kullanımı için avantajlı bir özellik olduğunu göstermektedir. MBNP'lerin geniş emilim spektrumu göz önüne alındığında, PTT deneylerinde kullanılmak üzere üç farklı dalga boyu (530 nm, 660 nm ve 785 nm) seçildi. Test edilen dalga boyları arasında yalnızca 785 nm ışınlama, hücre canlılığında önemli bir azalmaya yol açtı. Şelatlanmamış MNP'lar için hücre sağkalımı, 20 dakika PTT tedavisinden sonra yaklaşık %50'ye düştü. MNP-Fe^{3+} için sağkalım, 10 dakika PTT tedavisinde yaklaşık %40'a düştü ve 20 dakika PTT tedavisi ardından yaklaşık %30'a geriledi. Canlı/ölü boyama yalnızca 785 nm grubu için gerçekleştirildi ve MTT deneyinde gözlemlenen hücre ölümü modellerini doğruladı. Sonuçlar Fe^{3+} şelasyonunun MNP'lerin fototermal aktivitesini artırdığını gösterdi. Bu bulgular, MRI kontrastını arttırdığı bilinen MNP'lerin Fe^{3+} şelatlanmasının, biyouyumluluklarını ve PTT etkinliklerini iyileştirdiğini düşündürmektedir.

Anahtar Sözcükler: Melanin Nanoparçacıklar, Fe^{3+} şelatlanmış Melanin Nanoparçacıklar, Fototermal Terapi

TABLE OF CONTENTS

ACKNOWLEDGMENTS . . . iii
ACADEMIC ETHICS AND INTEGRITY STATEMENT . . . iv
ABSTRACT . . . v
ÖZET . . . vi
LIST OF FIGURES . . . ix
LIST OF TABLES . . . xi
LIST OF SYMBOLS . . . xii
LIST OF ABBREVIATIONS . . . xiii
1. INTRODUCTION . . . 1
1.1 Motivation and Objectives . . . 1
1.1.1 Wavelength-Dependent Photothermal Performance . . . 2
1.1.2 Impact of Iron Chelation on Photothermal Efficiency . . . 3
2. BACKGROUND . . . 4
2.1 Prostate Cancer (PC) . . . 4
2.2 PTT: Mechanism and Key Requirements . . . 6
2.3 Photothermal Agents (PTAs) . . . 7
2.4 Melanin Nanoparticles (MNPs) . . . 8
3. MATERIALS and METHODS . . . 12
3.1 Synthesis of MBNPs . . . 12
3.2 Dispersion of MBNPs . . . 12
3.3 Characterization of MBNPs . . . 13
3.4 Absorbence of MBNPs . . . 14
3.5 Cell Culture . . . 14
3.6 Cytotoxicity Assay . . . 15
3.7 PTT Experiment . . . 17
3.8 Live/Dead Staining . . . 19
3.9 Statistical Analysis . . . 20
4. RESULTS . . . 21
4.1 Characterization of MBNPs . . . 21

4.1.1 Dynamic Light Scattering (DLS) Analysis 21
4.1.2 Fourier-Transform Infrared Spectroscopy (FTIR) 22
4.1.3 Scanning Electron Microscopy (SEM) 23
4.2 Absorbence of MBNPs 25
4.3 Cytotoxicity Assay 25
4.4 PTT Experiment 26
4.5 Live/Dead Staining 28
5. DISCUSSIONS 31
6. CONCLUSIONS 36
REFERENCES 37

LIST OF FIGURES

Figure 1.1 Schematic illustration of experimental process. First, ink is extracted from the cuttlefish, followed by the synthesis of MNPs. Next, the MNPs are incubated with cells. Finally, the MNPs accumulated by the cells are irradiated with a laser, resulting in cell death. 2

Figure 2.1 Mechanism of PTT (1) PTA injection (2) PTA distribution in the body and accumulation in the tumor area (3) Irradiation of the tumor area with a light source (4) Healing of the tumor area. 7

Figure 3.1 (a) Image of 1 mg/mL MBNPs stock solution after 3 hours of ultrasonic bath (b) Image of 200 µg/mL diluted MBNPs solution (left: MNPs, right: MNP-Fe^{3+}). 13

Figure 3.2 PC-3 cells at around 75% confluency. Scale bar: 200 µm. 15

Figure 3.3 Experimental design for dark cytotoxicity assay of (a) MNPs and (b) MNP-Fe^{3+} on PC-3 cells. 16

Figure 3.4 Experimental plan for dark cytotoxicity assay. 16

Figure 3.5 Experimental design for PTT assay on PC-3 cells. 17

Figure 3.6 Experimental setup for PTT (a) 530 nm (b) 660 nm (c) 785 nm. 18

Figure 3.7 Experimental plan for PTT experiment. 19

Figure 3.8 Experimental plan for live/dead cell staining assay. 20

Figure 4.1 DLS analysis of (a) MNPs and (b) MNP-Fe^{3+}. 21

Figure 4.2 FTIR spectrum of (a) MNPs and (b) MNP-Fe^{3+}. 23

Figure 4.3 SEM images of MNPs. Scale bar: 1 µm and 200 nm, respectively. 24

Figure 4.4 SEM images of MNP-Fe^{3+}. Scale bar: 500 nm and 400 nm, respectively. 24

Figure 4.5 Size distribution graph for (a) MNPs and (b) MNP-Fe^{3+}. 24

Figure 4.6 Absorbence of MNPs and MNP-Fe^{3+}. 25

Figure 4.7 PC-3 cell survival after incubation with differentbou concentrations (a) MNPs and (b) MNP-Fe^{3+} for 24 hours. Each group was compared to the non-treatment (NT) group. Significant differences ($p<0.05$) were shown by an asterisk. 26

Figure 4.8 PC-3 cell survival at 785 nm PTT with (a) MNPs and (b) MNP-Fe^{3+}. PTT groups were compared to the non-treatment (NT) group. Significant differences ($p<0.05$) were shown by an asterisk. (ns:non-significant). 27

Figure 4.9 PC-3 cell survival at 530 nm PTT with (a) MNPs and (b) MNP-Fe^{3+}. Each group was compared to the non-treatment (NT) group. (ns:non-significant). 27

Figure 4.10 PC-3 cell survival at 660 nm PTT with (a) MNPs and (b) MNP-Fe^{3+}. Each group was compared to the non-treatment (NT) group. (ns:non-significant). 28

Figure 4.11 Fluorescence images of the 10-min 785 nm PTT group for (a) MNPs and (b) MNP-Fe^{3+}. Scale bar: 200 µm. 29

Figure 4.12 Fluorescence images of the NT group under 785 nm for (a) MNPs and (b) MNP-Fe^{3+}. Scale bar: 200 µm. 29

Figure 4.13 Fluorescence images of the light-only group under 785 nm for (a) MNPs and (b) MNP-Fe^{3+}. Scale bar: 200 µm. 30

Figure 4.14 Fluorescence images of the Np-only Group under 785 nm for (a) MNPs and (b) MNP-Fe^{3+}. Scale bar: 200 µm. 30

LIST OF TABLES

Table 3.1 PTT Parameters: Wavelength, Power Density, and Irradiation Time. 18

Table 4.1 DLS Data: Z-Average, and Polydispersity Index. 21

LIST OF SYMBOLS

CO_2	Carbon Dioxide
Cu^{2+}	Copper
Fe^{3+}	Iron
Gd^{3+}	Gadolinium
Mn^{2+}	Manganese
mL	Milliliter
mg/mL	Milligram per milliliter
min	Minute
mW	Milliwatt
mW/cm^2	Milliwatts per Square Centimeter
nm	Nanometer
rpm	Revolutions per Minute
µg/mL	Microgram per Milliliter
µM	Micromolar
W	Watt
W/cm^2	Watt per Square Centimeter

LIST OF ABBREVIATIONS

ACS	American Cancer Society
ADT	Androgen Deprivation Therapy
ANOVA	Analysis of Variance
ATCC	American Type Culture Collection
DI Water	Distilled Water
DLS	Dynamic Light Scattering
DMEM	Dulbecco's Modified Eagle Medium
DMSO	Dimethyl Sulfoxide
DOX	Doxorubicin
EthD-1	Ethidium Homodimer-1
MNP-Fe^{3+}	Fe^{3+}-chelated MNPs
FTIR	Fourier-Transform Infrared Spectroscopy
HIFU	High-Intensity Focused Ultrasound
ICD	Immunogenic Cell Death
ICG	Indocyanine Green
LED	Light Emitting Diode
MBNP	Melanin-Based Nanoparticle
MNP	Melanin Nanoparticle
MRI	Magnetic Resonance Imaging
MTT	3-(4,5-Dimethylthiazol-2-yl)-2,5-Diphenyltetrazolium Bromide
NIR	Near-Infrared
PBS	Phosphate-Buffered Salin
PDA	Polydopamine
PDI	Polydispersity Index
PEG	Polyethylene Glycol
Pen-Strep	Penicillin-Streptomycin
PC	Prostate Cancer
PC-3	Prostate Cancer Cell Line

PDT	Photodynamic Therapy
PTA	Photothermal Agents
PTT	Photothermal Therapy
RBC	Red Blood Cell
SEM	Scanning Electron Microscopy

1. INTRODUCTION

Cancer is one of the most common causes of death in the world. The 2025 report from the American Cancer Society (ACS) estimates over two million new cancer cases and six thousand cancer deaths to occur in the United States. Among various types, lung, breast, colorectal, prostate, stomach, and cervical cancers represent the most common and life-threatening forms [1].

The increasing occurrence of cancer, resultant from variables such as older populations, lifestyle choices, environmental exposures, and genetic susceptibilities, drives the need for continued cancer research. While conventional cancer treatments such as chemotherapy, radiotherapy, and surgery remain the mainstay of clinical management, their lack of selectivity and associated systemic side effects often limit their overall therapeutic success. These limitations have driven the search for alternative approaches, including light-based treatment, such as PTT, which offer targeted and less invasive treatment strategies [2]. Consequently, there is growing interest in developing biocompatible and efficient nanostructures to enhance the selectivity and efficacy of these emerging modalities.

1.1 Motivation and Objectives

MNPs chelated with metal ions have been explored for theranostic (diagnosis+treatment) applications; however, the effect of metal ion chelation on PTT performance has not been fully elucidated. The goal of this study is to evaluate photothermal performance of non-chelated and Fe^{3+}-chelated MNPs derived from natural sources (*cuttlefish*) for potential use in PTT. By systematically examining the influence of light wavelength and metal ion chelation on photothermal efficiency, the study seeks to identify key parameters affecting PTT performance. Figure 1.1 schematically illustrates the experimental process with MNPs.

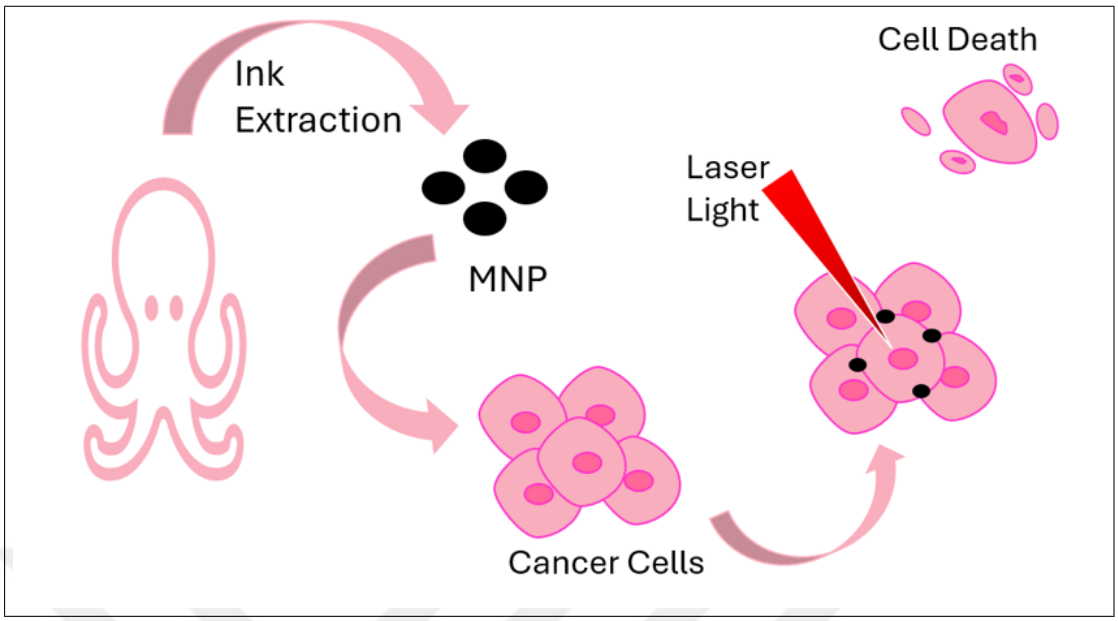

Figure 1.1 Schematic illustration of experimental process. First, ink is extracted from the cuttlefish, followed by the synthesis of MNPs. Next, the MNPs are incubated with cells. Finally, the MNPs accumulated by the cells are irradiated with a laser, resulting in cell death.

1.1.1 Wavelength-Dependent Photothermal Performance

Light-tissue interactions and the photothermal response of nanoparticles vary significantly with wavelength, as different wavelengths penetrate tissues to different depths and are absorbed to varying degrees by different materials [3],[4]. This study assessed the photothermal therapeutic potential of MBNPs at three wavelengths, 530 nm, 660 nm, and 785 nm, by evaluating their effect on the viability of the PC-3. Both non-chelated and Fe^{3+}-chelated MNPs were compared to determine how wavelength-dependent absorption influences photothermal efficiency and cell-killing capacity.

1.1.2 Impact of Iron Chelation on Photothermal Efficiency

Incorporation of metal ions, including gadolinium (Gd^{3+}), manganese (Mn^{2+}), copper (Cu^{2+}), and iron (Fe^{3+}), into the melanin structure can significantly alter its electronic configuration, optical properties, thermal conductivity, and overall stability [5]. These modifications directly influence the heat-generation capacity of MNPs under light irradiation. In this study, Fe^{3+}-chelated MNPs were evaluated to determine how iron incorporation modifies their photothermal performance.

2. BACKGROUND

2.1 Prostate Cancer (PC)

PC is among the most frequently diagnosed malignancies in men worldwide and continues to represent a significant global public health challenge. According to the 2024 data from the ACS, approximately 300,000 new prostate cancer cases were projected in the USA, with over 35,000 deaths. These figures highlight the persistent burden of prostate cancer despite advances in medical science and healthcare delivery [6].

PC is typically characterized by slow progression, which often allows the disease to remain asymptomatic during its early stages. However, if left undetected or untreated, it can advance to stages that result in severe complications, including local invasion and distant metastases [7]. The primary risk factors associated with prostate cancer include advancing age, racial background (with higher prevalence among African American men), genetic predisposition, dietary habits, obesity, history of venereal diseases, smoking, and levels of physical activity [7],[8].

PC diagnosis typically begins with evaluating serum prostate-specific antigen levels, often combined with digital rectal examination, as initial screening tools. When these evaluations increase clinical suspicion, additional imaging modalities, i.e., transrectal ultrasound and MRI, are used to identify suspicious lesions and direct tissue sampling. Definitive diagnosis, however, relies on histopathological confirmation obtained through prostate biopsy, which remains the gold standard. While these diagnostic strategies have markedly improved early detection rates, a critical challenge persists in distinguishing clinically significant, aggressive tumors from indolent forms of the disease, which may not require immediate intervention. This limitation underscores the need for more precise biomarkers and diagnostic tools to stratify disease risk and guide appropriate therapeutic decisions accurately [9],[10].

Treatment for localized prostate cancer includes surgery and radiation therapy [8]. For advanced cases of the disease when it has spread, hormonal treatments such as androgen deprivation therapy (ADT) are used to lower the levels of testosterone in the bloodstream, preventing the cancer cells from growing and multiplying [11]. Despite the efficacy of these traditional treatment approaches, they are often accompanied by substantial side effects and complications that can decrease the patient's quality of life. Common complications include urinary incontinence, sexual dysfunction, and gastrointestinal issues, which necessitate a careful evaluation of treatment options tailored to individual patient needs [12].

Considering these challenges, there is an increasing emphasis on developing novel therapeutic strategies that minimize side effects and improve functional outcomes. Advances in targeted therapies, immunotherapy, and minimally invasive techniques are promising avenues for reducing the burden of prostate cancer treatment on patients while maintaining or improving therapeutic efficacy [13].

Minimally invasive techniques have garnered significant attention as potential alternatives to conventional prostate cancer treatments due to their ability to avoid complications and uphold a high standard of life for the patient. Among these, cryotherapy, high-intensity focused ultrasound (HIFU), PDT, and PTT have emerged as innovative and promising techniques [14]. Cryotherapy involves the controlled application of extreme cold to ablate cancerous tissue, while HIFU uses precisely targeted ultrasound waves to generate localized heat, leading to tumor destruction [15]. PDT utilizes photosensitizing compounds to increase reactive species that selectively kill malignant cells, while PTT directly converts light energy into heat, enabling precise and localized tumor ablation [16].

2.2 PTT: Mechanism and Key Requirements

PTT has emerged as a cutting-edge therapeutic approach, offering a minimally invasive and highly targeted solution for various medical applications, particularly bacterial infection management and cancer therapy. Using light-absorbing agents to generate heat, PTT achieves selective damage to diseased tissues with minimal impact on surrounding healthy cells [16]. This precision makes PTT an attractive alternative or complementary method to conventional therapies such as surgery, chemotherapy, and radiotherapy. A key benefit of PTT lies in its capacity to offer accurate spatial and temporal regulation throughout therapy, ensuring localized and efficient therapeutic outcomes [17],[18].

The PTT mechanism involves using photothermal agents (PTAs), which absorb light energy, typically in the NIR spectrum, and convert it into heat through non-radiative relaxation or plasmonic effects. When the localized temperature rises above 42 °C, irreversible thermal damage to targeted tissues occurs, effectively destroying cancer cells or pathogenic bacteria [11]. To maximize the efficacy of PTT, PTAs must possess several key properties, including low biotoxicity, high photothermal conversion efficiency, stability under physiological conditions, and compatibility with biological systems [16],[18]. Figure 2.1 summarizes the PTT mechanism.

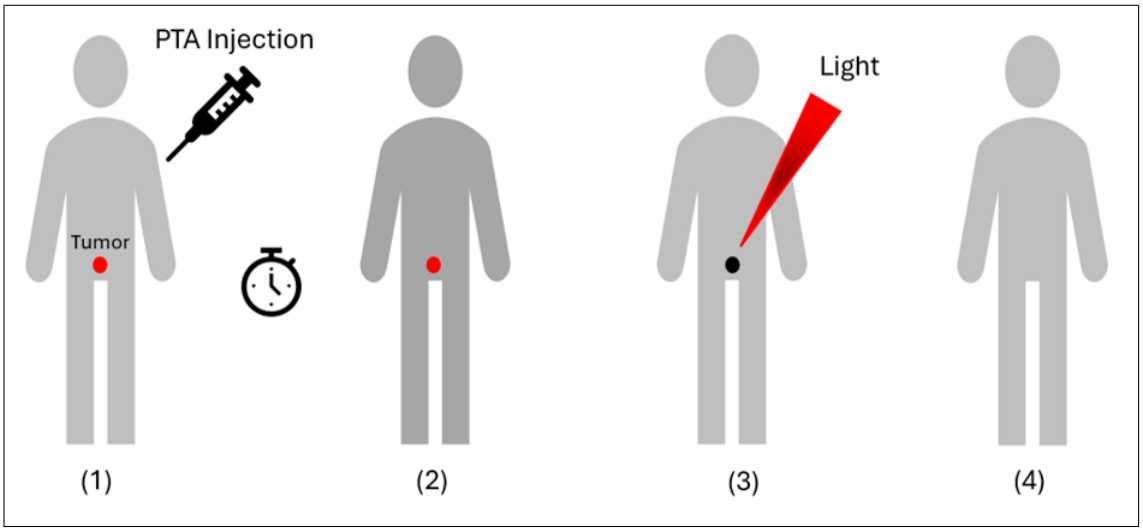

Figure 2.1 Mechanism of PTT (1) PTA injection (2) PTA distribution in the body and accumulation in the tumor area (3) Irradiation of the tumor area with a light source (4) Healing of the tumor area.

2.3 Photothermal Agents (PTAs)

PTAs are generally classified into two major categories: inorganic and organic nanomaterials, each offering distinct advantages and application potential. Inorganic PTAs, including noble metal-based nanoparticles like gold nanorods, copper chalcogenide semiconductors like CuS, carbon-based nanostructures like graphene, and two-dimensional materials like black phosphorus nanosheets, are known for their excellent photothermal stability and strong NIR absorbance, making them highly effective for tumor ablation. However, concerns about long-term toxicity and biodegradability limit their clinical application [17],[19]. In contrast, organic PTAs typically offer enhanced safety and biodegradability, making them more suitable for biomedical applications where biocompatibility is critical. Small molecule organic fluorophores such as indocyanine green (ICG) and naturally occurring polymers like melanin are particularly promising due to their favorable biological profiles, including reduced toxicity, inherent biodegradability, and good NIR absorption capabilities [17],[20].

2.4 Melanin Nanoparticles (MNPs)

Melanin is a biopolymer that is widely distributed across various biological systems, including mammalian eyes, skin, and hair, as well as in pathological conditions such as melanoma. Beyond mammals, melanin is also found in a diverse range of marine organisms, including cuttlefish (*Sepia officinalis*) and octopuses, where it plays a crucial role in pigmentation, camouflage, and protection against environmental stressors. Additionally, melanin is present in plants and certain microorganisms, contributing to defense mechanisms against UV radiation, oxidative stress, and microbial attacks [21],[22].

Depending on the source and synthesis method, MNPs can be classified as natural or synthetic. Synthetically produced MNPs, most notably polydopamine (PDA), mimic the structure and function of natural MNPs and offer superior control over size, morphology, and surface chemistry, enabling consistent and tunable nanoparticle synthesis [21]. PDA is synthesized through the oxidative self-polymerization of dopamine in a mildly alkaline environment (pH $\approx$ 7,5), and it is easier to synthesize than natural MNPs [23]. Like naturally derived MNPs, PDA exhibits strong broadband optical absorption in the NIR region, enabling effective photothermal conversion for applications such as PTT [24]. In addition, PDA contains abundant catechol and amine functional groups on its surface, allowing for versatile chemical modifications including metal ion chelation (e.g., Gd^{3+}, Mn^{2+}, Fe^{3+}, and Cu^{2+}), drug loading, or conjugation with targeting ligands. These surface properties make PDA an ideal nanoplatform for multifunctional cancer imaging, diagnosis, and therapy applications. Due to these numerous advantages, PDA frequently appears in literature as a key material in many studies involving MNPs [5],[25].

Liu et al. demonstrated that PDA colloidal nanospheres possess high potential as safe photothermal agents, showing no adverse effects on cell viability. Moreover, in vivo experiments revealed no significant systemic toxicity or organ damage following PDA administration. Under laser irradiation at 808 nm (2 W/cm^2 for 500 s), a temperature increase of approximately 37 °C was achieved at a PDA concentration

of 200 µg/mL, with a photothermal conversion efficiency reaching %40. These findings highlight the strong promise of PDA as a biocompatible and effective agent for photothermal therapy [26].

Dong et al. developed a multifunctional nanoplatform based on PDA by co-loading multiple agents, including ICG, doxorubicin (DOX), and Mn^{2+}. The system demonstrated a significant photothermal effect after exposure to an 808 nm NIR laser at varying power densities (100, 300, and 400 mW/cm^2 for 20 min). Moreover, the Mn^{2+} ions chelated to the PDA surface provided enhanced contrast in T_1-weighted MRI, enabling real-time monitoring of the therapeutic process. With its dual capability of delivering combinational therapeutics and enabling multimodal imaging, this PDA-based theranostic platform holds great promise for precision oncology and personalized cancer treatment strategies [27].

Kang et al. designed a multifunctional nanoplatform based on melanin-like polydopamine (poly(L-DOPA)) nanoparticles chelated with Mn^{2+} ions, which demonstrated potential for combined photothermal and photodynamic cancer therapy, as well as T_1- weighted MRI contrast. Under 808 nm laser irradiation (1.2 W/cm^2 for 20 min), the nanoparticle solution at a concentration of 200 µg/mL reached a temperature of approximately 72 °C, indicating significant photothermal effects due to strong NIR absorption. Experimental data from both cell culture and animal models showed that this platform is biocompatible, effective, and capable of targeted delivery, highlighting its potential as a promising theranostic agent [28].

Natural MNPs, typically derived from biological sources such as cuttlefish ink, human hair, or certain fungi, are increasingly being investigated for biomedical applications due to their favorable biological interactions, degradability, and antioxidant properties [24]. Among their most notable physicochemical features is the ability to absorb light across a broad spectral range, particularly in the NIR, and efficiently convert this energy into heat. This photothermal conversion capability stems from their unique chemical structure, which is composed of polyphenolic compounds with monomeric indole rings. These conjugated structures support broadband optical ab-

sorption and contribute to free radical scavenging and redox activity, enhancing their multifunctionality in biological environments. Due to their high absorption in the NIR region, MNPs have garnered significant interest in PTT, facilitating effective light-to-heat conversion for targeted tumor ablation with minimal invasiveness [23],[24]. Furthermore, their optical properties enable the use of MNPs as efficient contrast agents in photoacoustic imaging (PAI) [24]. Additionally, the surface chemistry of melanin allows for functionalization with metal ions (Gd^{3+}, Mn^{2+}, Cu^{2+}, and Fe^{3+}, thereby imparting paramagnetic characteristics that enhance MRI contrast and broaden their applicability in neuroimaging and multimodal diagnostic platforms [5]. Given its broad functional versatility, melanin holds great promise as a biocompatible and sustainable material for next-generation PTT strategies, with potential applications extending beyond oncology to drug delivery, antioxidative protection, and regenerative medicine.

Li et al. utilized natural MNPs extracted from Sepia ink and coated them with cancer cell membranes to construct a biomimetic photothermal therapeutic platform targeting breast cancer. Upon irradiation with an 808 nm laser (2 W/cm^2 for 500s), the MNPs at a concentration of 150 µg/mL induced a temperature increase up to approximately 60°C, corresponding to a high photothermal conversion efficiency of 40%. This treatment resulted in strong cytotoxic effects, reducing cell viability to below 15%. Beyond effective tumor suppression, it also triggered immunogenic cell death (ICD), promoting antitumor immune responses. These findings highlight the dual function of naturally derived MNPs as efficient PTAs and immunomodulatory components, broadening their application potential in combinatorial cancer therapies such as PTT combined with immunotherapy [29].

Kim et al. coated melanin nanoparticles derived from natural sources with polyethylene glycol (PEG) to improve their dispersibility in physiological environments and injected them into the tail vein of 4T1 tumor-bearing mice. Following irradiation with an 808 nm laser (1.5 W/cm^2 for 7 min), the temperature of the tumor region increased to approximately 48 °C. Cell cytotoxicity experiments revealed that tumor growth was reduced to less than 50% compared to the control group. Moreover, in vitro and in vivo experiments demonstrated that the nanoparticles were biocompatible

and showed no cytotoxic effects under physiological conditions. These results highlight the potential of naturally derived MBNPs as effective and minimally invasive agents for cancer treatment via PTT [30].

Jiang et al. developed a Melanin@RBC system by coating melanin nanoparticles extracted from cuttlefish ink with red blood cell (RBC) membranes to enhance biocompatibility and prolong circulation, promoting better tumor accumulation. Upon irradiation with an 808 nm laser (2 W/cm^2 for 5 min), the system's temperature exceeded 60 °C within 500 seconds, achieving a photothermal conversion efficiency of approximately 40%. Moreover, tumor accumulation was observed through PAI. This study highlights the potential of naturally derived MNPs to serve as multifunctional platforms for effective photothermal therapy and diagnostic imaging, making them promising candidates for theranostic applications [31].

Chen et al. studied ions including Fe^{3+}, Mn^{2+}, Cu^{2+}, and Gd^{3+} on the contrast performance of endogenous MNPs in MRI. The results show that metal-chelated MNPs exhibited negligible toxicity and high biodegradability. The study highlighted the potential of these nature-inspired materials as efficient metal-chelating MRI contrast agents. These findings support the feasibility of using melanin as a multifunctional platform, particularly for MRI-guided therapeutic applications [32].

While biologically derived MNPs offer numerous advantages, it is important to note that their isolation and purification can be more challenging compared to synthetic counterparts, due to the presence of biological impurities and batch-to-batch variability. Therefore, carefully considering source and processing methods is essential for ensuring consistency and reproducibility in such applications.

3. MATERIALS and METHODS

3.1 Synthesis of MBNPs

MBNPs used in this study were synthesized from cuttlefish (*Sepia officinalis*) ink. Following a previously reported protocol, the ink was washed with DI water 5 times and then centrifuged at 10,000 rpm (20 minutes). The resulting pellet was collected and subsequently dried to obtain the melanin nanoparticles [33]. According to a previously reported protocol, 100 µL of Fe^{3+} solution (1 mg/mL) was added dropwise to 10 mL of MNP solution (1 mg/mL). To ensure complete chelation, the mixture was stirred continuously for three hours, followed by centrifugation at 10,000 rpm [34]. The Department of Biomedical Engineering at Bahçeşehir and Izmir Democracy University collaborated o this part of the study. Therefore, the MNPs were synthesized at Bahçeşehir University and provided in a ready-to-use form.

3.2 Dispersion of MBNPs

Distilled (DI) water is the solvent for MBNPs, so it was used throughout the study for stock preparation and characterization analyses. 1 mg/mL stock solution was subjected to an ultrasonic bath for approximately 3 hours before use to ensure uniform dispersion and prevent nanoparticle agglomeration. Figure 3.1 (a) shows non-cheleated and Fe^{3+}-chelated MNPs after 3 hours of ultrasonic bath, and Figure 3.1 (b) shows 200 µg/mL diluted MNP solution. As illustrated in Figure 3.1, both the stock and diluted solutions of MNPs exhibit an intense black coloration.

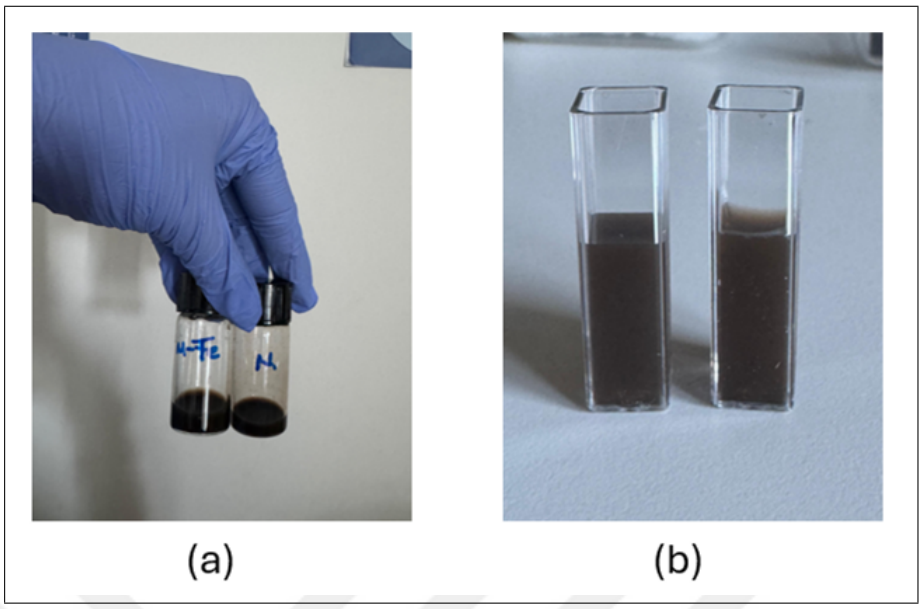

Figure 3.1 (a) Image of 1 mg/mL MBNPs stock solution after 3 hours of ultrasonic bath (b) Image of 200 µg/mL diluted MBNPs solution (left: MNPs, right: MNP-Fe^{3+}).

3.3 Characterization of MBNPs

The synthesized nanoparticles were thoroughly analyzed through Scanning Electron Microscopy (SEM), Dynamic Light Scattering (DLS), and Fourier Transform Infrared Spectroscopy (FTIR) techniques, allowing assessment of their structure, particle size distribution, and surface chemical composition.

SEM is a powerful imaging technique that provides detailed surface morphology and topographical information by scanning the sample with a focused beam of electrons. To assess nanoparticle size distribution in suspension, DLS measures temporal variations in scattered light resulting from their Brownian motion. FTIR was conducted in Attenuated Total Reflectance (ATR) mode to investigate the composition of the nanoparticles and their surface functional groups by detecting characteristic vibrational modes of molecular bonds. All these characterization analyses were performed through service procurement from the Life Sciences Center at Boğaziçi University.

Obtaining a homogeneous and transparent nanoparticle suspension is essential to ensure accurate imaging and measurement in SEM and DLS analyses. For SEM analysis, 10 µg/mL of the MNP stock solution was taken. 1 mL was diluted in DI water. A drop of the resulting suspension was then placed onto SEM sample stubs and allowed to dry for approximately 3 h under ambient conditions. A similar preparation method was followed for DLS analysis. 10 µg/mL of the MNP stock solution was diluted with 1 mL of DI water. The sample prepared was then transferred into a cuvette suitable for DLS measurement.

3.4 Absorbence of MBNPs

To obtain the absorbance spectra of non-chelated and Fe^{3+}-chelated MNPs, nanoparticles were diluted to 100 µg/mL in DI water. Spectrophotometer cuvettes (optical path length: 1 cm) were used at room temperature. A UV-Vis spectrophotometer (Nanodrop 2000c) was used to acquire the absorbance spectra of the nanoparticles at the 200-800 nm range.

3.5 Cell Culture

The prostate cancer cell line (PC-3) was selected as the in vitro model in this study. Cancer research widely uses these cells to study late-stage disease progression, metastasis, and treatment resistance [35]. Therefore, PC-3 cells provide a valuable platform for investigating the potential anticancer effects of novel nanoparticle-based treatments. PC-3 cells were cultured according to the instructions provided by the American Type Culture Collection (ATCC). Cells were maintained in culture media DMEM supplemented with 10% Fetal Bovine Serum (FBS) and 1% Penicillin-Streptomycin (Pen-Strep) solution to support cell growth and prevent bacterial contamination. To mimic physiological conditions, cells were cultured at 37 °C in a CO_2-enriched (5%) humidified incubator. Culture medium was replaced regularly until the cells reached

approximately 75% confluence. Once the desired confluency was achieved, as shown in Figure 3.2, the cells were either passaged or harvested for experimental use using a Trypsin-EDTA solution.

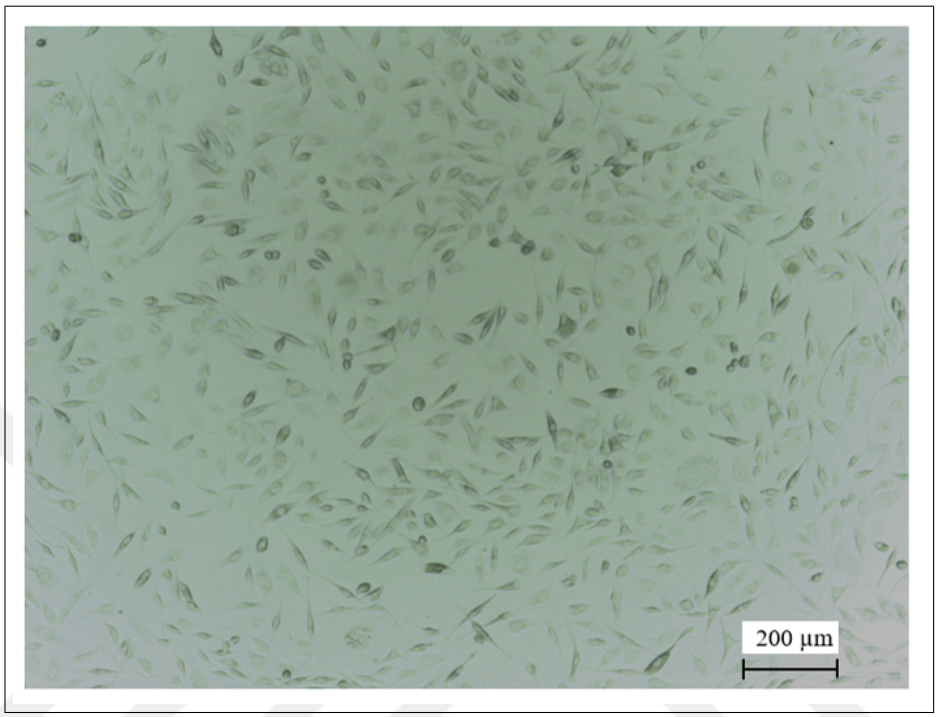

Figure 3.2 PC-3 cells at around 75% confluency. Scale bar: 200 µm.

3.6 Cytotoxicity Assay

To determine the cytotoxicity of the synthesized nanoparticles prior to photothermal activation, a dark toxicity experiment was conducted on PC-3 cells using the MTT assay. A seeding density of 10,000 PC-3 cells per well was used in 96-well plates, followed by a 24-hour incubation to promote cell attachment. Subsequently, the cells were exposed to varying doses (50 to 500 µg/mL) of two nanoparticle formulations: non-chelated and Fe^{3+}-chelated MNPs, followed by an additional 24-hour incubation period in standard culture conditions as illustrated in Figure 3.3.

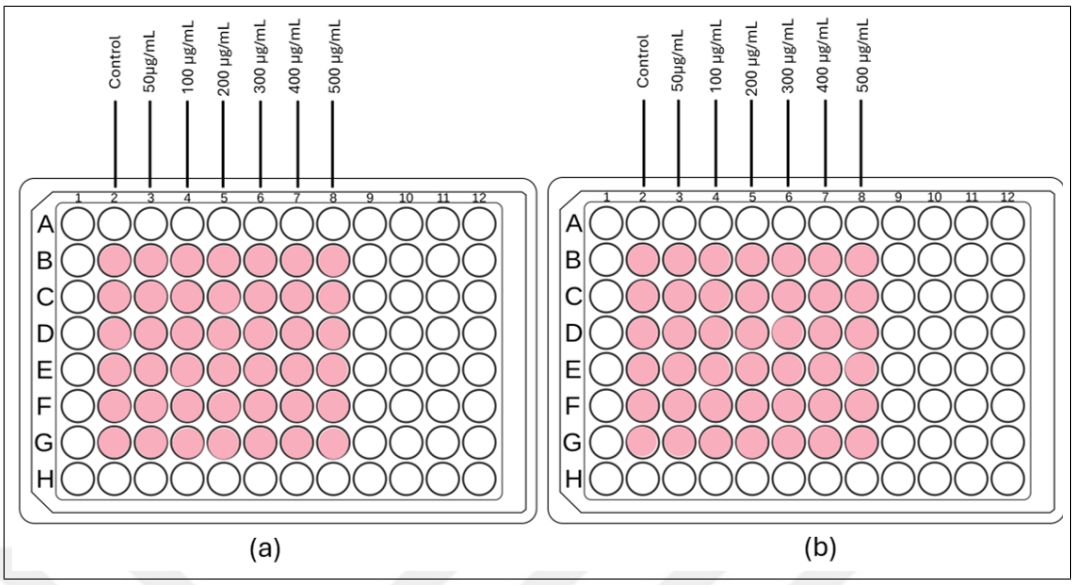

Figure 3.3 Experimental design for dark cytotoxicity assay of (a) MNPs and (b) MNP-Fe^{3+} on PC-3 cells.

Following the 24-hour nanoparticle incubation period, the media were removed, and the cells were washed three times with Phosphate-Buffered Saline (PBS) to eliminate any residual nanoparticles that could interfere with the MTT reaction. The MTT reagent was then added to each well at a volume equivalent to 10% of the total medium volume. The plates underwent a 3-hour incubation at standard culture conditions to enable the formazan crystal formation by metabolically active cells. After discarding the culture medium, Dimethyl Sulfoxide (DMSO) was added to dissolve the resulting crystal. Absorbance measurements at 570 nm were taken using a microplate reader, and the viability of treated cells was compared with that of the non-treatment group. Each treatment group was tested in six technical replicates, and the entire experiment was repeated in triplicate to ensure statistical validity. Figure 3.4 represents a general overview of the experimental timeline for the dark cytotoxicity experiment.

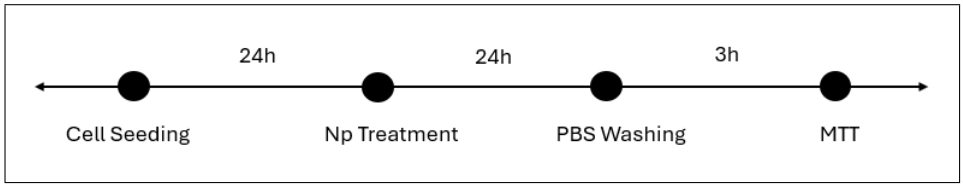

Figure 3.4 Experimental plan for dark cytotoxicity assay.

3.7 PTT Experiment

As illustrated in Figure 3.5, PC-3 cells were seeded into 96-well plates in a circular arrangement, consisting of five experimental groups, each occupying four wells. After a 24-hour incubation period to allow cell attachment, 200 µg/mL MNPs were added to the relevant groups. The cells were then incubated for an additional day.

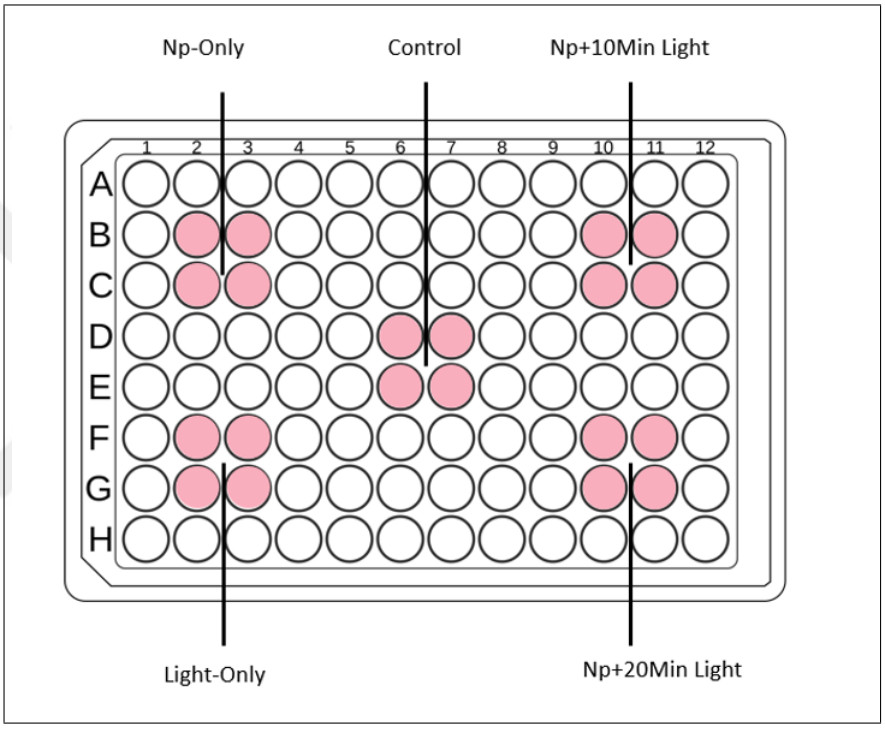

Figure 3.5 Experimental design for PTT assay on PC-3 cells.

Following this incubation, wells were washed with PBS before refreshing the culture medium. The medium in the control and light-only group was also refreshed to ensure consistency across all groups prior to irradiation.

As shown in Figure 3.6, light sources with different wavelengths, 530 nm and 660 nm LEDs, and 785 nm laser were used for the PTT experiment. Before irradiation, each light source was set to operate at its maximum output power to ensure consistent and efficient energy delivery. Accordingly, the power output of the 530 nm LED was

200 mW, the 660 nm LED was 400 mW, and the 785 nm laser delivered 1 W. Table 3.1 summarizes the wavelengths, power densities, and irradiation times of the lasers used in this study. Power densities were calculated by dividing the power output by the spot size. In this study, the spot size was defined as the area illuminated by the light source, which covered four wells. Each well had a diameter of 1 cm, and the total illuminated region was considered circular with a radius of 1 cm, resulting in a spot size of approximately 3.14 cm^2 ($A = \pi r^2,\ \pi \approx 3.14$).

To maintain a constant physiological temperature during irradiation, a hot plate was preheated to 37 °C and used as a base for the well plates. The nanoparticle-treated groups were exposed to light for 10 and 20 minutes, while the light-only group was irradiated for 20 minutes.

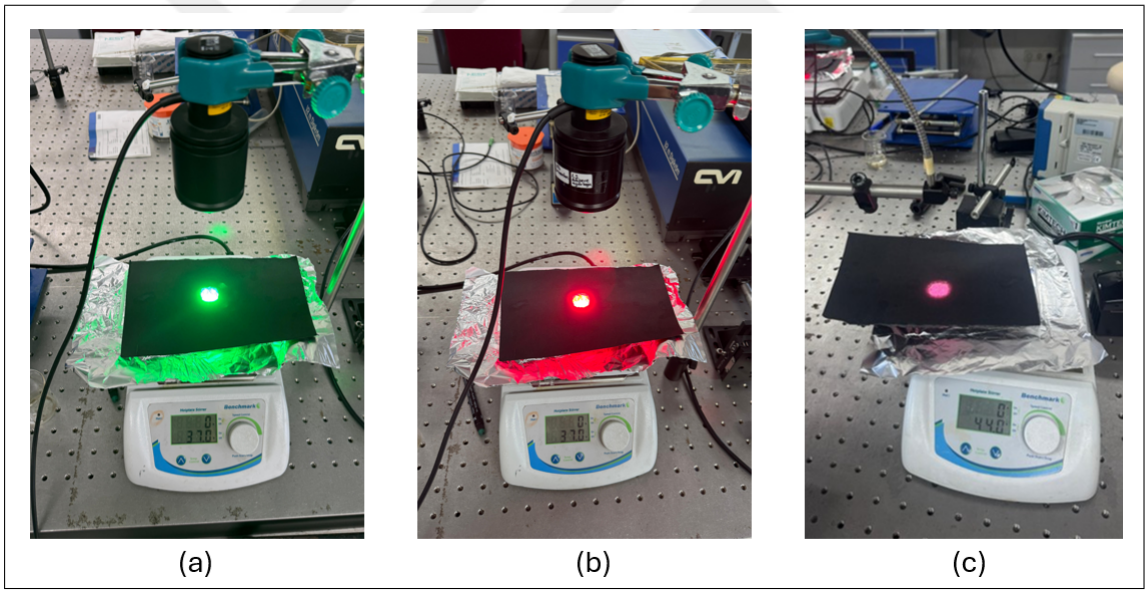

Figure 3.6 Experimental setup for PTT (a) 530 nm (b) 660 nm (c) 785 nm.

Table 3.1
PTT Parameters: Wavelength, Power Density, and Irradiation Time.

Wavelength (nm)	Power Density (mW/cm^2)	Irradiation Time (min)
530	65	10 and 20
660	130	10 and 20
785	350	10 and 20

After laser irradiation, the plates were incubated for an other day. Subsequently, each well received MTT reagent at a volume corresponding to 10% of the overall medium volume. A 3-hour incubation period was applied to the well plates to promote the generation of formazan crystals by metabolically active cells. Afterwards, the medium was discarded, and DMSO was used to dissolve the crystals. Absorbance readings at 570 nm were conducted with a microplate reader, and cell viability was assessed against control groups. Figure 3.7 illustrates a general overview of the experimental timeline for the PTT experiment.

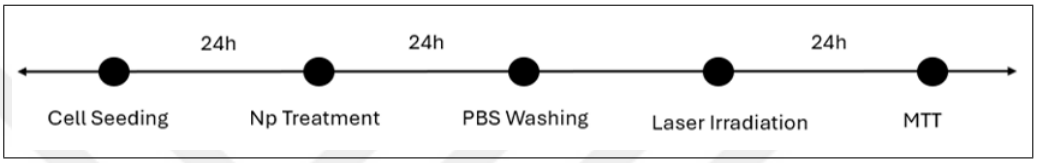

Figure 3.7 Experimental plan for PTT experiment.

3.8 Live/Dead Staining

To visualize the viability of PC-3 cells following PTT at 785 nm, a live/dead staining assay was conducted using a viability/cytotoxicity kit. Calcein-AM is enzymatically converted by intracellular esterases in viable cells, producing green fluorescence, whereas Ethidium Homodimer-1 (EthD-1) penetrates only cells with compromised membranes, binding to nucleic acids and emitting red fluorescence.

In this experiment, cells were exposed to 785 nm laser irradiation for 10 minutes, selected based on prior PTT studies showing significant cell death even at this shorter duration. After laser exposure, plates were incubated for another day. On the following day, cells were incubated with a staining solution consisting of 2 µM Calcein-AM and 8 µM EthD-1 in 4 mL of PBS for 30 minutes at room temperature in the dark. Fluorescence images were obtained after the 30-minute staining incubation. Figure 3.8 shows a general overview of the experimental timeline for live/dead staining assay.

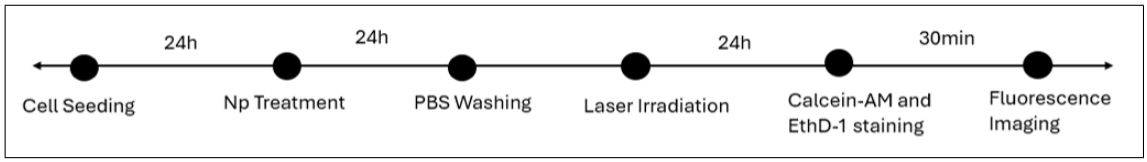

Figure 3.8 Experimental plan for live/dead cell staining assay.

3.9 Statistical Analysis

Data normality was confirmed prior to statistical analysis. To compare means across groups, one-way analysis of variance (ANOVA) was employed, followed by Tukeyâs test for detailed multiple comparisons. Significance was set at 5% ($p < 0.05$), and notable differences were indicated by an asterisk (*) in figures. Experiments were conducted in triplicate.

4. RESULTS

4.1 Characterization of MBNPs

4.1.1 Dynamic Light Scattering (DLS) Analysis

The results of DLS analysis revealed that synthesized MNPs exhibited a Z-average hydrodynamic diameter of approximately 194.6 nm, with a narrow polydispersity index (PDI) of 0.0971, indicating a highly monodisperse size distribution. In comparison, Fe^{3+}-chelated MNPs showed a slightly increased Z-average size of 218.9 nm, while the PDI decreased to 0.0484, suggesting an even narrower size distribution and improved colloidal uniformity upon Fe^{3+} chelation. The outcomes of the DLS analysis are presented in Figure 4.1 and Table 4.1 below.

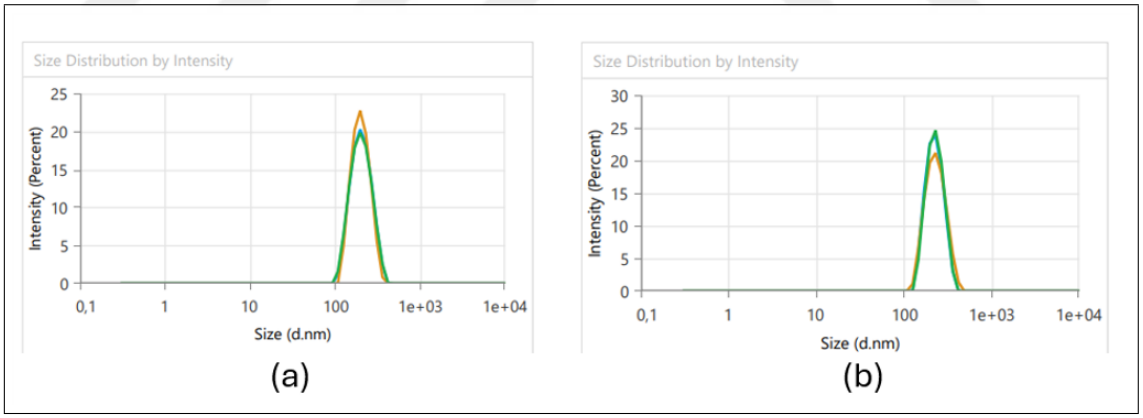

Figure 4.1 DLS analysis of (a) MNPs and (b) MNP-Fe^{3+}.

Table 4.1
DLS Data: Z-Average, and Polydispersity Index.

Nanoparticles	Z-Average (nm)	Polydispersity Index (PDI)
MNPs	194,6	0,0971
MNPs-Fe	218,9	0,04839

4.1.2 Fourier-Transform Infrared Spectroscopy (FTIR)

The FTIR spectrum of the squid-derived MNPs reveals characteristic absorption bands consistent with the presence of key functional groups associated with natural melanin. A broad absorption band is observed around ≈3400 cm^{-1} corresponds to O-H and N-H stretching vibrations, indicating the presence of hydroxyl and amine groups. The peak near 1620 cm^{-1} is attributed to the C=O stretching of carboxylic acid and/or aromatic C=C stretching vibrations, typical of the indole and catechol moieties in melanin. Absorptions in the region of 1400-1500 cm^{-1} are associated with C-N stretching vibrations, while the band around 1100 cm^{-1} may arise from C-O stretching, suggesting the presence of phenolic or ether groups. These spectral features confirm the complex, heterogeneous structure of the melanin polymer and support its biogenesis. FTIR spectrum of MNPs is presented in Figure 4.2 (a).

The FTIR spectrum of Fe^{3+}-chelated MNPs exhibits a high degree of similarity to that of non-chelated melanin, suggesting that the primary chemical structure of melanin is largely preserved upon chelation. Nevertheless, minor spectral variations imply partial coordination of Fe^{3+} ions with specific functional groups within the melanin matrix. The broad absorption band around ≈3400 cm^{-1}, attributed to O-H and N-H stretching vibrations, remains present but displays a slight shift and reduced intensity, indicative of potential involvement of hydroxyl and/or amine groups in metal binding. A subtle shift in the peak near 1620 cm^{-1}, corresponding to C=O and aromatic C=C stretching modes, further supports weak interactions between iron ions and carbonyl or aromatic moieties. Additionally, the bands observed in the 1400-1500 cm^{-1} region, assigned to C-N and C-O stretching vibrations, show minor changes in both position and intensity, which may be ascribed to localized electronic perturbations induced by Fe^{3+} coordination. Furthermore, the appearance of a weak absorption band around 680 cm^{-1} is consistent with Fe-O stretching vibrations, providing supplementary evidence for the formation of Fe-O bonds within the chelated structure. FTIR spectrum of MNP-Fe^{3+} is presented in Figure 4.2 (b).

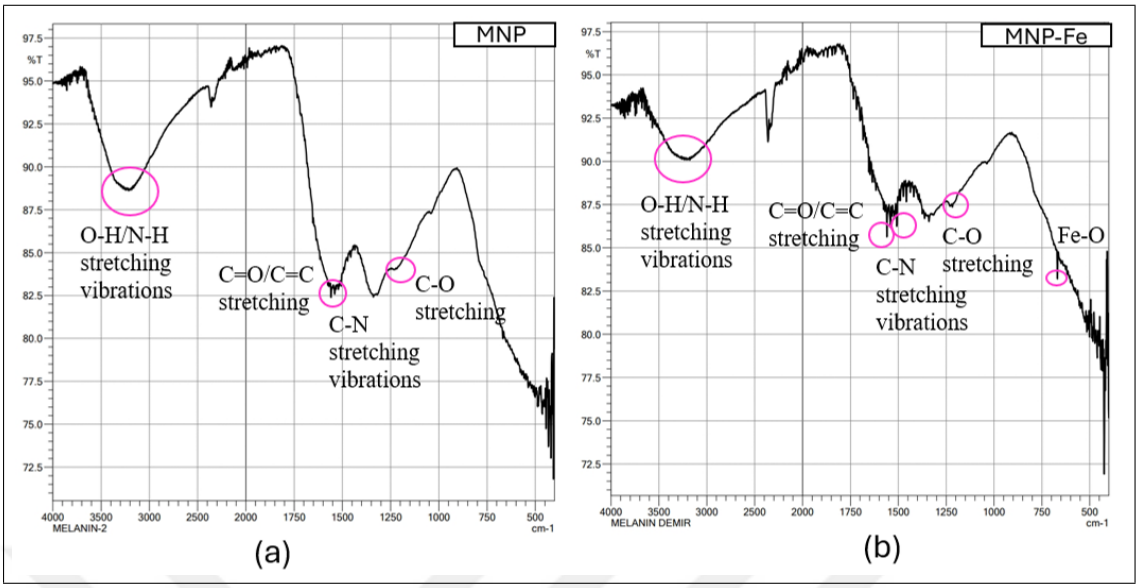

Figure 4.2 FTIR spectrum of (a) MNPs and (b) MNP-Fe^{3+}.

4.1.3 Scanning Electron Microscopy (SEM)

SEM images revealed that both non-chelated and Fe^{3+}-chelated MNPs exhibited a spherical morphology with a uniform distribution, indicating successful and consistent nanoparticle formation as illustrated in Figures 4.3 and 4.4. Furthermore, histogram analyses derived from SEM images were conducted to assess the particle size distribution of both non-chelated and Fe^{3+}-chelated MNPs. The data revealed that the majority of particles in both samples clustered within a defined size range, indicating a relatively homogeneous morphology. The average particle size for the non-chelated MNP group was approximately 160 nm, whereas the MNP-Fe^{3+} group exhibited an average size of 194 nm. Figure 4.5 represents the size distribution graph for non-chelated and Fe^{3+}-chelated MNP groups.

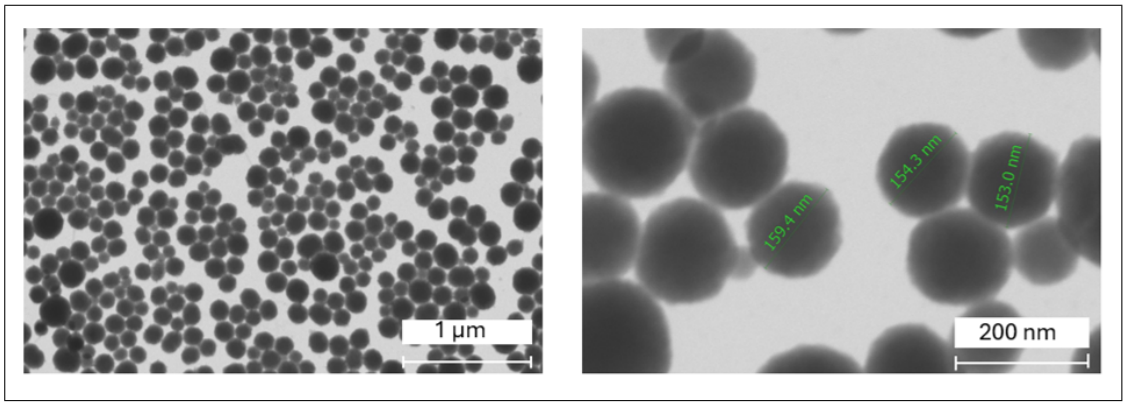

Figure 4.3 SEM images of MNPs. Scale bar: 1 µm and 200 nm, respectively.

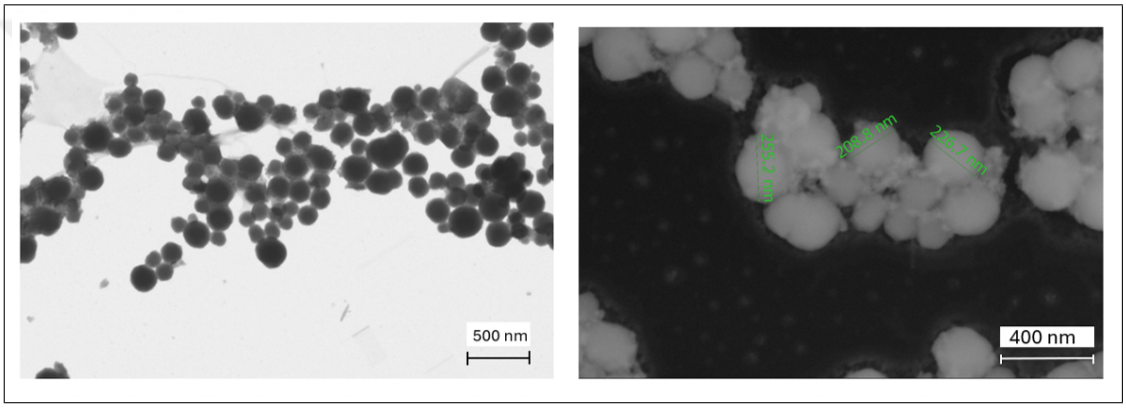

Figure 4.4 SEM images of MNP-Fe^{3+}. Scale bar: 500 nm and 400 nm, respectively.

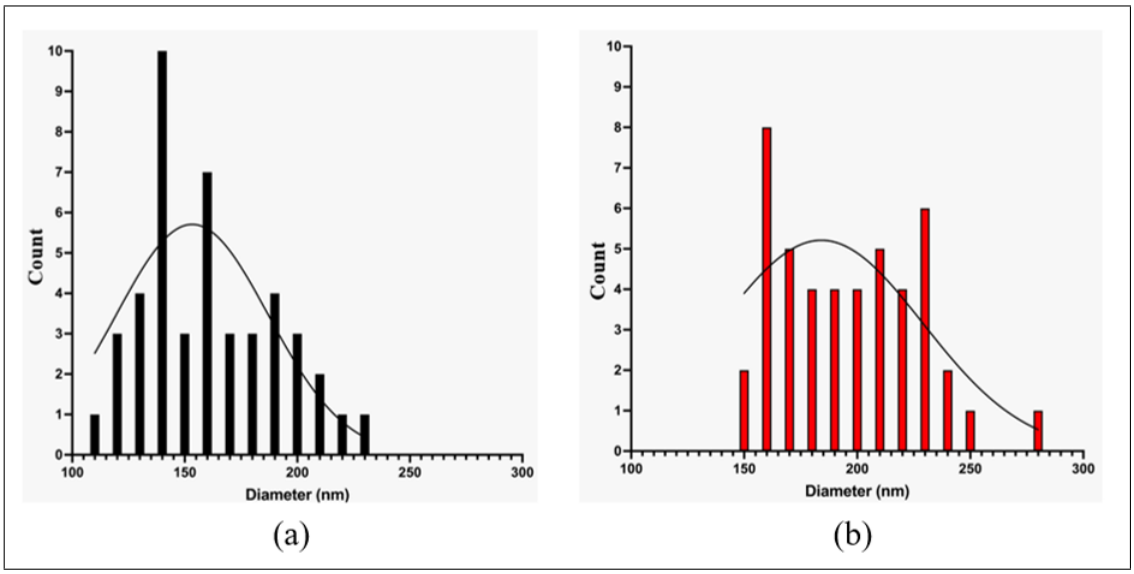

Figure 4.5 Size distribution graph for (a) MNPs and (b) MNP-Fe^{3+}.

4.2 Absorbence of MBNPs

As shown in Figure 4.6, both non-chelated and Fe^{3+}-chelated MNPs exhibited broad absorbance profiles extending from UV to NIR region (200-800 nm). Both types of nanoparticles exhibited a broad-spectrum absorbance profile throughout the measurement range. This characteristic broadband optical property was a determining factor in the decision to use three different light sources (530 nm, 660 nm, and 785 nm) in the PTT experiments. The non-chelated MNPs exhibited higher absorbance values compared to Fe^{3+}-chelated MNPs, particularly in the 300-500 nm region.

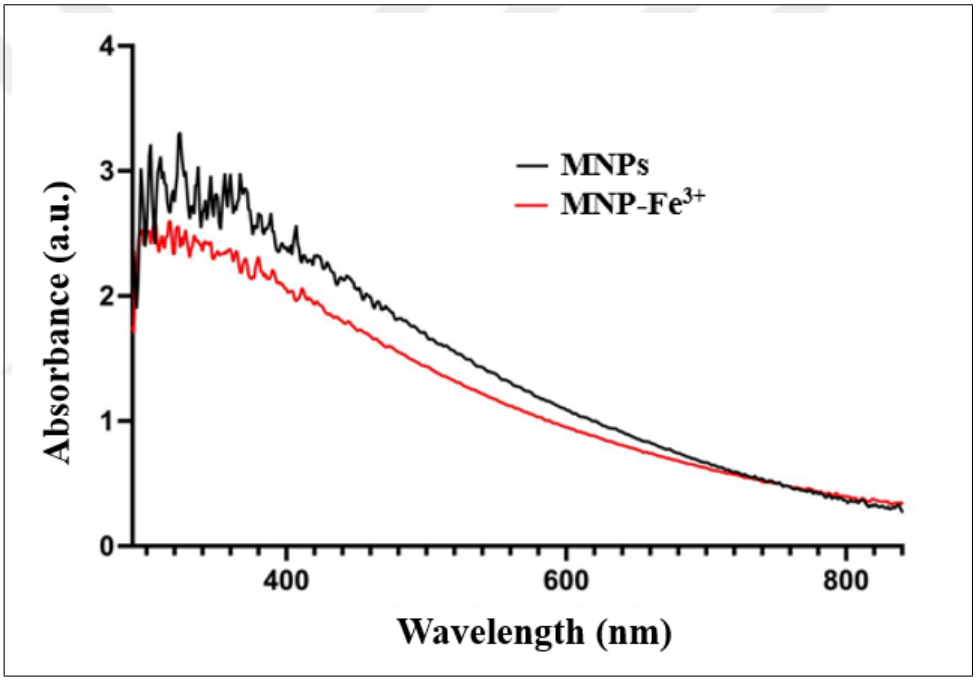

Figure 4.6 Absorbence of MNPs and MNP-Fe^{3+}.

4.3 Cytotoxicity Assay

As shown in Figure 4.7, the MTT assay results across different concentrations revealed that the nanoparticles did not exhibit significant cytotoxicity up to 200 µg/mL, with cell viability remaining above 80% at these doses. Although Fe^{3+}-chelated MNPs followed a similar trend, the decrease in viability at higher concentrations was less pronounced and did not reach statistical significance. In order to ensure a meaningful and

standardized comparison between non-chelated and Fe^{3+}-chelated MNPs in subsequent PTT experiments, a concentration of 200 µg/mL was selected for both groups. This concentration was considered optimal as it represented the highest dose with minimal inherent cytotoxicity while also providing a common baseline for evaluating PTT across both nanoparticle types.

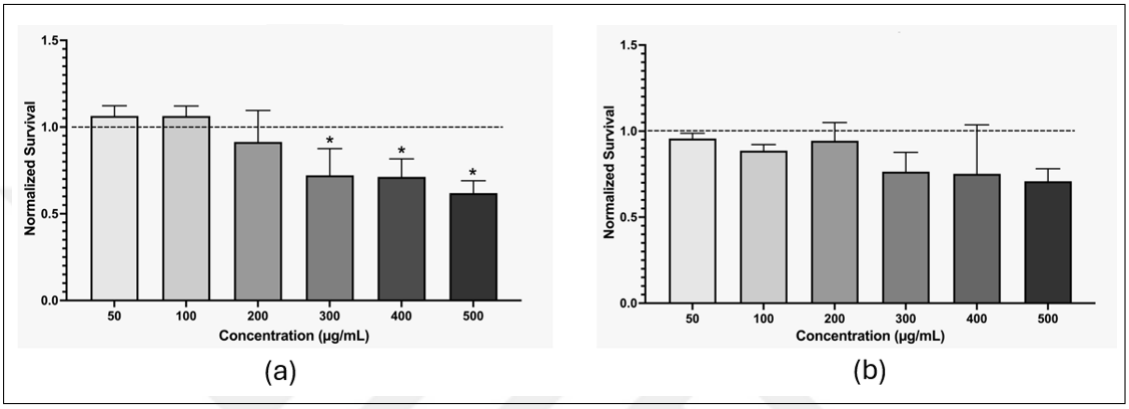

Figure 4.7 PC-3 cell survival after incubation with differentbou concentrations (a) MNPs and (b) MNP-Fe^{3+} for 24 hours. Each group was compared to the non-treatment (NT) group. Significant differences ($p<0.05$) were shown by an asterisk.

4.4 PTT Experiment

As shown in Figure 4.8, PTT experiments conducted at 785 nm demonstrated significant cytotoxicity for both non-chelated MNPs and Fe^{3+}-chelated MNPs. Fe^{3+}-chelated MNPs reduced PC-3 cell survival to approximately 30% following 20-minute PTT treatment, while non-chelated MNPs yielded about 50% viability after 20-minute PTT treatment, indicating that iron chelation may further improve the photothermal efficacy. The PTT results demonstrated that the 20-minute PTT treatment resulted a higher rate of cell death relative to the 10-minute PTT treatment. Nevertheless, the observed variation did not reach statistical significance. Conversely, NT, Np-only, and Light-only groups did not exhibit a significant reduction in cell viability, demonstrating that neither the nanoparticles nor the laser alone induced cytotoxicity.

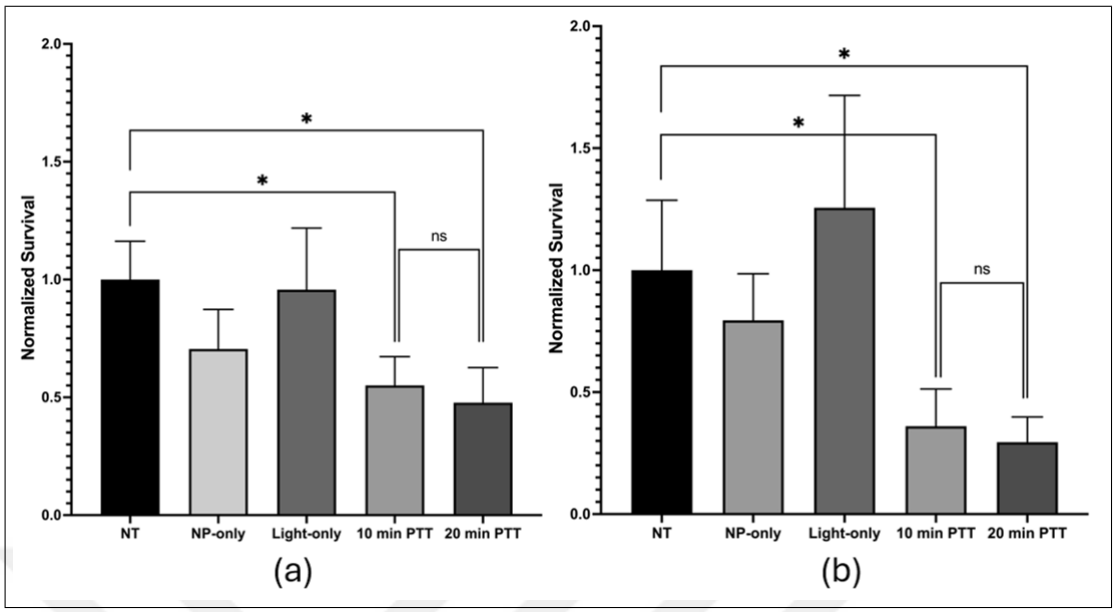

Figure 4.8 PC-3 cell survival at 785 nm PTT with (a) MNPs and (b) MNP-Fe^{3+}. PTT groups were compared to the non-treatment (NT) group. Significant differences ($p<0.05$) were shown by an asterisk. (ns:non-significant).

Furthermore, PTT experiments conducted using LED light sources at 530 nm (Figure 4.9) and 660 nm (Figure 4.10) did not produce significant cytotoxic effects in either non-chelated or Fe^{3+}-chelated MNPs when compared to the NT group.

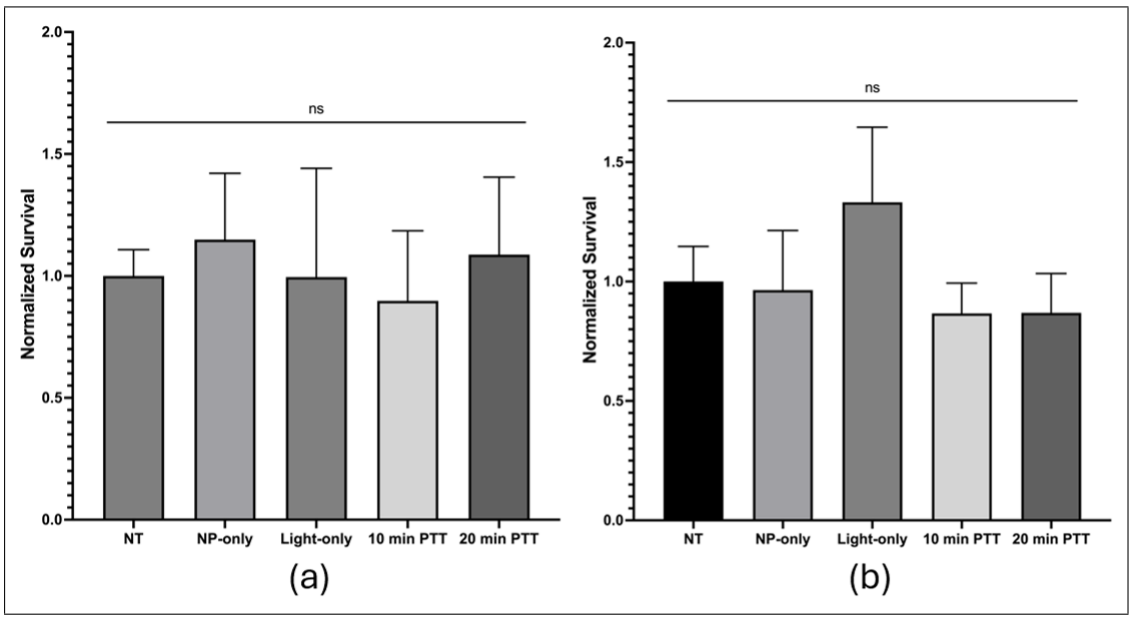

Figure 4.9 PC-3 cell survival at 530 nm PTT with (a) MNPs and (b) MNP-Fe^{3+}. Each group was compared to the non-treatment (NT) group. (ns:non-significant).

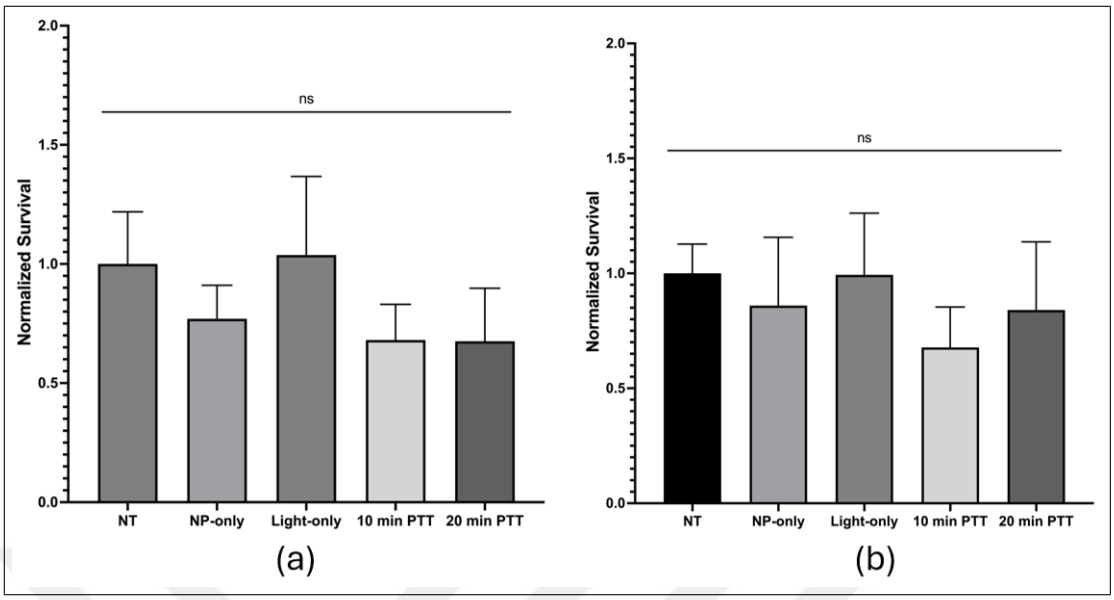

Figure 4.10 PC-3 cell survival at 660 nm PTT with (a) MNPs and (b) MNP-Fe^{3+}. Each group was compared to the non-treatment (NT) group. (ns:non-significant).

4.5 Live/Dead Staining

Calcein-AM and EthD-1 were performed only for the 785 nm irradiation group (10 min), as it was the only condition that resulted in significant cell death in the MTT assay. Figure 4.11 illustrates that PC-3 cells treated with MBNPs and subsequently exposed to 785 nm light exhibited intense red fluorescence, indicating substantial cell death. In contrast, the control group showed predominantly green fluorescence, reflecting high cell viability as shown in Figure 4.12. Cells exposed to either light-only (Figure 4.13) or nanoparticles-only (Np-only) (Figure 4.14) also demonstrated mainly green fluorescence, similarly to the control group. These findings are consistent with MTT assay results and further support the PTT efficacy of MBNPs under 785 nm irradiation. It is important to note that the experiment was repeated once, so it was ultimately considered a preliminary investigation.

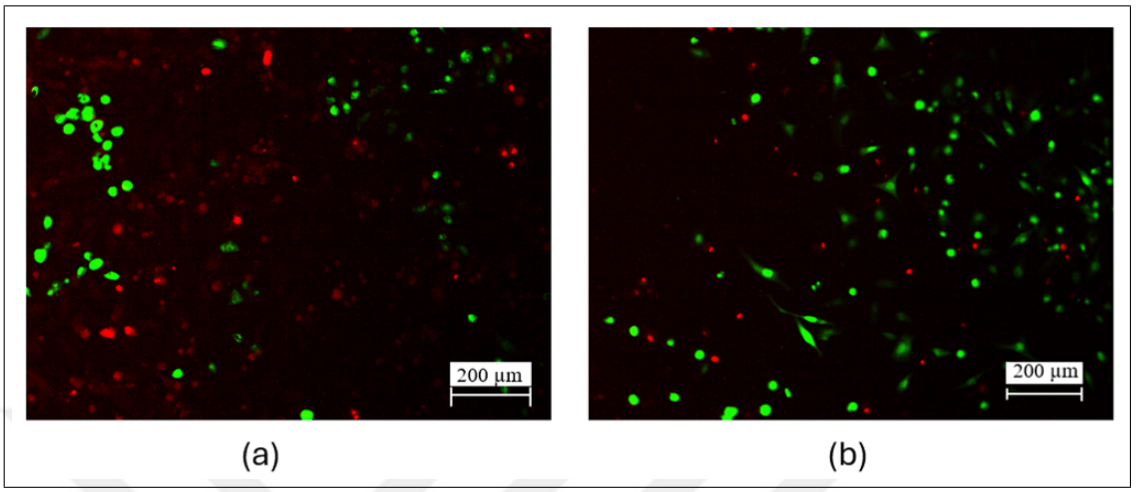

Figure 4.11 Fluorescence images of the 10-min 785 nm PTT group for (a) MNPs and (b) MNP-Fe^{3+}. Scale bar: 200 µm.

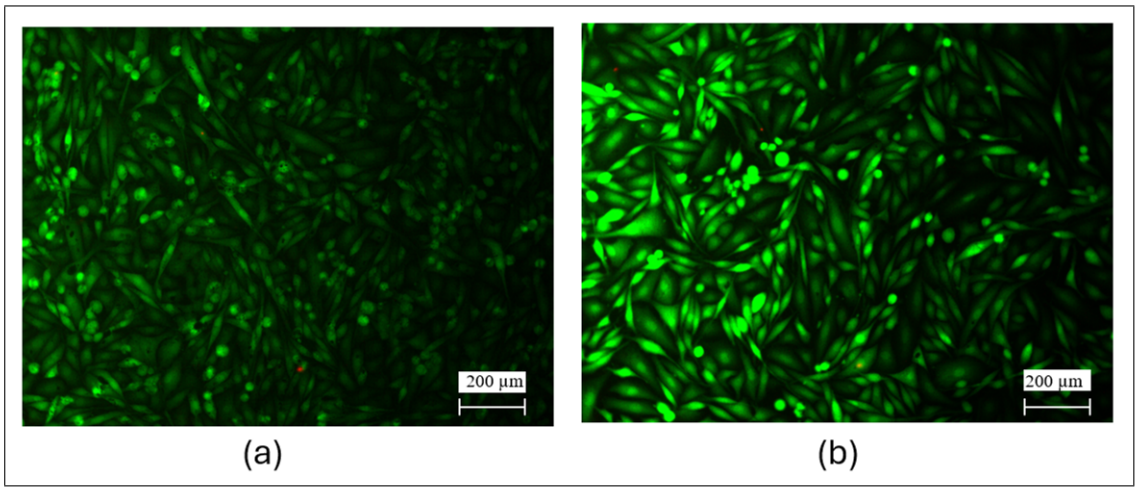

Figure 4.12 Fluorescence images of the NT group under 785 nm for (a) MNPs and (b) MNP-Fe^{3+}. Scale bar: 200 µm.

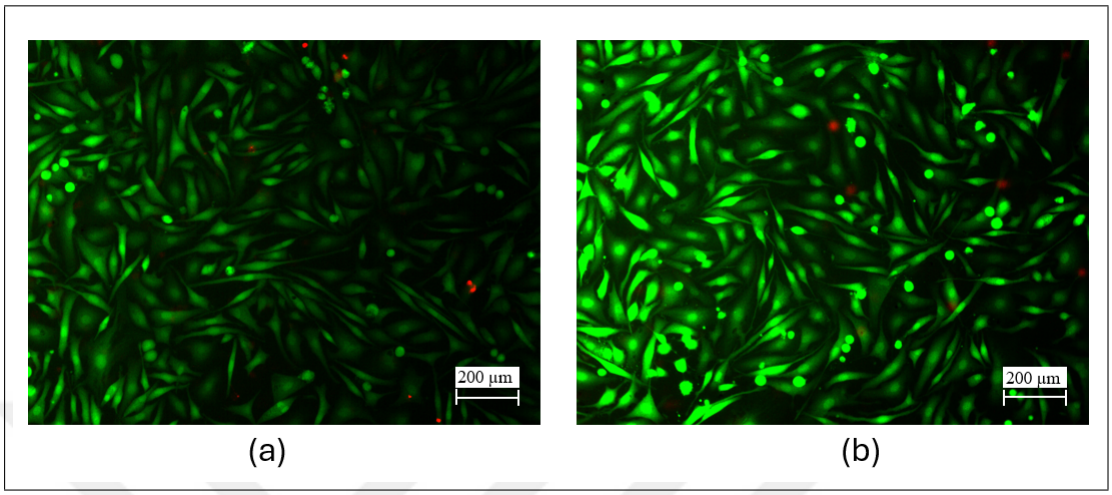

Figure 4.13 Fluorescence images of the light-only group under 785 nm for (a) MNPs and (b) MNP-Fe^{3+}. Scale bar: 200 µm.

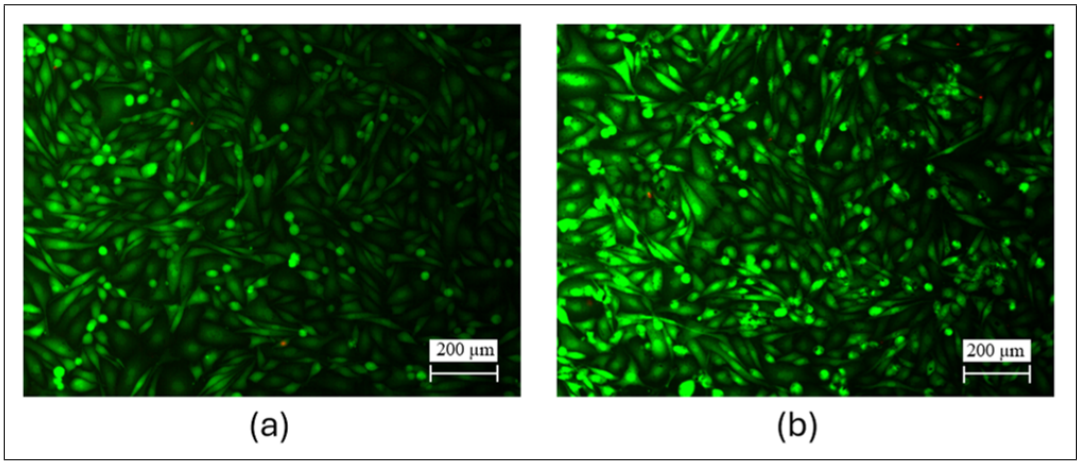

Figure 4.14 Fluorescence images of the Np-only Group under 785 nm for (a) MNPs and (b) MNP-Fe^{3+}. Scale bar: 200 µm.

5. DISCUSSIONS

In this study, the photothermal therapeutic potential of MBNPs was investigated. Our primary objectives were to compare the effects of both non-chelated and Fe^{3+}-chelated MNPs on the PC-3 under irradiation at different laser wavelengths (530 nm, 660 nm, and 785 nm), and to determine the most effective laser wavelength for PTT). Additionally, we aimed to elucidate the impact of Fe^{3+} chelation on the photothermal performance of these nanoparticles.

Comprehensive characterization of both the non-chelated MNPs and the Fe^{3+}-chelated MNPs was performed using SEM, FTIR, and DLS analyses. SEM images revealed that both types of nanoparticles exhibited homogeneous and spherical morphology with narrow size distributions in the nanometer range. The non-cheleted MNPs synthesized in this study showed an average size of approximately 155 nm by SEM and 194.6 nm by DLS, with a low polydispersity index (0.0971), indicating uniform size distribution and good colloidal stability. Li et al. [29] reported nanoparticle sizes between 130-150 nm by TEM and a hydrodynamic diameter of 235 ± 4 nm by DLS; Xu et al. [36] reported particle sizes around 190 nm by TEM and SEM with a size dispersity of 0.123; and Regan et al. [37] observed a z-average hydrodynamic diameter of 193 nm by DLS and an average diameter of 130 ± 3 nm with a standard deviation of 33 nm by TEM. The Fe^{3+}-chelated MNPs exhibited larger sizes (210 nm by SEM and 218.9 nm by DLS) and even lower PDI (0.0484). Liang et al. reported uniform solid spheres with slightly rough surfaces and an average size of approximately 200 nm by SEM and TEM [38]. These findings are consistent with the morphological and size characteristics of the non-chelated and Fe^{3+}-chelated MNPs synthesized in this study, thus validating our results against the literature. The slight differences in nanoparticle sizes observed between TEM/SEM and DLS measurements may be attributed to factors such as the hydrated state measured by DLS, possible aggregation or surface roughness, as well as natural biological variability between individual Sepia specimens used in each synthesis. Given that live animals are used as the source, such interspecific differences in

nanoparticle size are expected. These findings confirm that the morphological and size characteristics of both non-chelated and Fe^{3+}-chelated MNPs synthesized in this study are consistent with those reported in the literature.

Both non-chelated and Fe^{3+}-chelated MNPs exhibited broad absorbance profiles covering the UV to NIR range. Non-chelated MNPs demonstrated higher absorbance values compared to their Fe^{3+}-chelated MNPs, particularly within the 300-500 nm spectral range. However, it should be noted that these measurements strongly depend on the preparation of the samples, such as weighing and completely dissolving the stocks. This characteristic broadband absorption behavior formed the rationale for selecting three distinct irradiation wavelengths (530 nm, 660 nm, and 785 nm) for PTT experiments with the aim of assessing the wavelength-dependent photothermal performance of the nanoparticles. Considering the high absorbance observed in the 300-500 nm region, a photothermal effect was expected at 530 nm for non-chelated and Fe^{3+}-chelated MNPs. However, no significant cytotoxic response was observed following 530 nm irradiation. This is most likely due to the limited power output (200 mW) of the 530 nm LED, which may have been insufficient to trigger an effective thermal response, despite the favorable optical properties of the nanoparticles at that wavelength.

In most studies in the literature, 808 nm lasers have been used to evaluate the photothermal effects of MBNPs. Li et al. observed that MNPs coated cancer cell membranes (150 µg/mL) associated caused strong cytotoxic effects, decreasing cell viability below 15% when irradiated with an 808 nm laser (2 W/cm^2, 500 seconds). In contrast, they found that neither laser irradiation nor MNPs alone induced significant toxicity. By comparison, although a relatively higher nanoparticle concentration (200 µg/mL) and a longer irradiation time (10 and 20 min), was used in our experiments, the lower power likely resulted in a higher cell viability (50%). These differences highlight the critical role of laser parameters, particularly power density, in determining the overall photothermal efficacy [29]. Kim et al. achieved approximately 50% tumor suppression in vivo using PEG-coated MNPs irradiated with an 808 nm laser (1.5 W/cm^2, 7 min). Similarly, in our in vitro experiments with uncoated MNPs, cell viability decreased to

about 50% after 20 minutes of exposure to a 785 nm laser. The comparable reduction in viability, despite differences in experimental models and irradiation parameters, underscores the potential of MNPs as effective photothermal agents [30].

While numerous studies have examined the chelation of Fe^{3+} with synthetic MNPs, such as PDA, to investigate photothermal effects, there is a significant lack of research focusing on Fe^{3+}-chelated MNPs derived from natural sources such as squid ink. Xu et al. demonstrated that Fe^{3+}-chelated polydopamine nanoparticles (Fe-PDA) showed superior photothermal tumor cell inhibition compared to non-chelated PDA when tested on 4T1 cells under 808 nm laser irradiation (1 W/cm^2, 15 min) [39]. Live/dead staining assays (Calcein-AM/PI) further supported their quantitative viability data, highlighting Fe-PDA's enhanced therapeutic performance. These findings are consistent with our own results, where Fe^{3+}-chelated MNPs also induced greater cytotoxicity than non-chelated MNPs. Collectively, these findings highlight the critical contribution of Fe^{3+} chelation to enhancement of PTT efficacy.

PTT efficacy of MBNPs was highest under 785 nm irradiation, corresponding to the NIR window, which is characterized by superior tissue penetration relative to the visible wavelengths of 530 nm and 660 nm. This enhanced penetration at 785 nm facilitates more efficient energy transfer to the nanoparticles, resulting in increased localized heating and enhanced cytotoxicity. In contrast, irradiation at 530 nm and 660 nm yielded limited PTT effects, attributable to both lower tissue penetration and technical limitations. Visible light wavelengths are more strongly absorbed and scattered by biological tissues, restricting their ability to penetrate deeper cellular layers [4],[40]. Furthermore, the power output of the 530 nm and 660 nm light sources (200 mW and 400 mW, respectively) was lower than that of the 785 nm laser (1 W). The combined effects of lower power and reduced penetration resulted in insufficient temperature elevation, thereby limiting PTT efficiency in these groups.

Live/dead cell viability analysis was performed exclusively for the 785 nm irradiation group using Calcein-AM and Ethidium Homodimer-1 staining, as this wavelength demonstrated significant cytotoxic effects in preliminary PTT assays. Fluorescence microscopy images revealed a marked increase in red-stained (dead) cells exclusively in the group treated with 785 nm laser irradiation and MBNPs, compared to the control, nanoparticle-only, and light-only groups. These results corroborated the quantitative metabolic viability data obtained from MTT assays. Collectively, these findings underscore the photothermal therapeutic potential of MBNPs when activated by NIR light.

This study also investigated the effect of Fe^{3+} chelation on the 785 nm-PTT performance of MBNPs. PTT using Fe^{3+}-chelated MNPs exhibited greater cytotoxicity compared to non-chelated MNPs. Cell viability decreased to approximately 40% at 10-minute PTT treatment ($p<0.05$) and 30% at 20-minute PTT treatment ($p<0.05$) in the Fe^{3+}-chelated MNPs groups ($p<0.05$). In contrast, non-chelated MNPs resulted in about 50% cell viability at 20-minute PTT treatment ($p<0.05$). These findings suggest that chelation of Fe^{3+} ions with melanin may improve photothermal efficiency. Previous studies have proposed that metal ion chelation, such as with Fe^{3+}, can modify the optical properties of melanin by narrowing its bandgap, thereby promoting more efficient heat generation upon irradiation [41],[42]. Nevertheless, the precise mechanisms underlying this enhancement require further investigation.

While the outcomes of this research appear promising, there are several noteworthy limitations to consider. First, all experiments were conducted in vitro using only the PC-3 cells. While in vitro models provide valuable preliminary insights into nanoparticle behavior and cytotoxic effects, they do not fully replicate the complex physiological environment of living organisms. Secondly, different cancer cell types may exhibit varying sensitivity to PTT due to differences in cellular morphology and size. Therefore, expanding future studies to include multiple cancer cell lines and, ultimately, in vivo models would offer a more comprehensive understanding. Thirdly, although three different wavelengths were investigated, the power densities across the light sources could not be standardized due to equipment limitations. Variations in

laser power hinder direct comparisons of photothermal efficacy. It is plausible that higher-powered 530 nm and 660 nm light sources could yield more pronounced cytotoxic effects.

Lastly, despite their inherent biocompatibility and multifunctional potential, Fe^{3+}-chelated natural MNPs remain insufficiently explored. Increasing research attention toward these systems, particularly in combination with imaging-guided strategies such as MRI, could accelerate their integration into clinically relevant photothermal cancer therapies. Their dual role as theranostics offers a promising direction for future studies.

Future studies should utilize such high-intensity light sources to ensure consistent power density across wavelengths and enable direct comparisons of photothermal performance. These improvements would allow for a more accurate assessment of wavelength-dependent photothermal efficiency in MBNPs. Moreover, the dual theranostic role of Fe^{3+}-chelated MNPs presents a promising avenue for future MRI-guided photothermal therapy studies, offering the potential for both precise tumor ablation and real-time imaging-based treatment monitoring.

6. CONCLUSIONS

In conclusion, this study investigated the PTT potential of MBNPs, both non-chelated and Fe^{3+} -chelated, under laser irradiation at 530 nm, 660 nm, and 785 nm. Comprehensive characterization using SEM, FTIR, and DLS confirmed the successful synthesis of stable, nanoscale particles with physicochemical properties consistent with those reported in the literature. UV-Vis spectrophotometric analysis revealed broad absorbance profiles spanning the UV to NIR range for both nanoparticle types; notably, Fe^{3+}-chelated MNPs exhibited significantly higher absorbance intensities in the 300-500 nm region. Among the tested wavelengths, 785 nm demonstrated the highest PTT efficiency. Fe^{3+}-chelated MNPs resulted in approximately 40% cell viability in the 10 min PTT treatment group ($p<0.05$), decreasing to around 30% in the 20 min PTT treatment group ($p<0.05$). Compared to other groups, non-chelated MNPs showed approximately 50% cell viability in the 20 min PTT treatment group ($p<0.05$). These findings were supported by MTT assay and fluorescence-based live/dead cell staining, which revealed significant cytotoxic effects under 785 nm irradiation.

Despite the promising results, the study is limited by the use of a single in vitro cancer model and non-standardized power outputs across wavelengths. Future studies should expand to include multiple cell lines, in vivo validation, and equalized power densities to enable more accurate assessment of wavelength-dependent effects. In addition to enhancing photothermal efficiency, Fe^{3+}-chelation may also enable the use of MBNPs as MRI contrast agents. This multifunctionality opens new avenues for integrating imaging and therapy, paving the way for MRI-guided PTT in future applications.

Overall, the findings clearly indicate that Fe^{3+}-chelated MNPs exhibit superior photothermally induced cytotoxicity compared to their non-chelated counterparts, particularly NIR light activation. This highlights the potential of Fe^{3+} chelation to enhance the effectiveness of MBNPs, underscoring their promise as a platform for PTT.

REFERENCES

1. Siegel, R. L., T. B. Kratzer, A. N. Giaquinto, H. Sung, and A. Jemal, "Cancer statistics, 2025," *CA: A Cancer Journal for Clinicians*, Vol. 75, no. 1, pp. 10–45, 2025.

2. Bhole, R., C. Bonde, P. Kadam, and R. Wavwale, "A comprehensive review on photodynamic therapy (pdt) and photothermal therapy (ptt) for cancer treatment," *Turkish Journal of Oncology*, Vol. 36, no. 1, pp. 125–132, 2021. Review article.

3. Chen, J., C. Ning, Z. Zhou, P. Yu, Y. Zhu, G. Tan, and C. Mao, "Nanomaterials as photothermal therapeutic agents," *Progress in Materials Science*, Vol. 99, pp. 1–26, 2019.

4. Niemz, M. H., *Laser-Tissue Interactions*, Vol. 322, Springer-Verlag Berlin Heidelberg, 3rd ed., 2007.

5. Larsson, B., and H. Tjälve, "Studies on the melanin-affinity of metal ions," *Acta Physiologica Scandinavica*, Vol. 104, no. 4, pp. 479–484, 1978.

6. Yang, C.-H., D. V. Barbulescu, L. Marian, M.-C. Tung, Y.-C. Ou, and C.-H. Wu, "High-intensity focus ultrasound ablation in prostate cancer: A systematic review," *Journal of Personalized Medicine*, Vol. 14, no. 12, p. 1163, 2024.

7. Rawla, P., "Epidemiology of prostate cancer," *World Journal of Oncology*, Vol. 10, no. 2, pp. 63–89, 2019.

8. Dunn, M. W., and M. W. Kazer, "Prostate cancer overview," *Seminars in Oncology Nursing*, Vol. 27, no. 4, pp. 241–250, 2011.

9. Borley, N., and M. R. Feneley, "Prostate cancer: Diagnosis and staging," *Asian Journal of Andrology*, Vol. 11, no. 1, pp. 74–80, 2009.

10. Descotes, J.-L., "Diagnosis of prostate cancer," *Asian Journal of Urology*, Vol. 6, no. 2, pp. 129–136, 2019.

11. Sharifi, N., J. L. Gulley, and W. L. Dahut, "Androgen deprivation therapy for prostate cancer," *JAMA*, Vol. 294, no. 2, pp. 238–244, 2005.

12. Xiao, J., M. Zhang, and D. Wu, "Side effects of prostate cancer therapies and potential management," *Journal of Biological Methods*, Vol. 11, no. 3, p. e99010018, 2024.

13. Sekhoacha, M., K. Riet, P. Motloung, L. Gumenku, A. Adegoke, and S. Mashele, "Prostate cancer review: Genetics, diagnosis, treatment options, and alternative approaches," *Molecules*, Vol. 27, p. 5730, 2022.

14. Moore, C., D. Pendse, and M. Emberton, "Photodynamic therapy for prostate cancer-a review of current status and future promise," *Nature Reviews Urology*, Vol. 6, pp. 18–30, 2009.

15. Aus, G., "Current status of hifu and cryotherapy in prostate cancer-a review," *European Urology*, Vol. 50, no. 5, pp. 927–934, 2006.

16. Wilson, B. C., and R. A. Weersink, "The yin and yang of pdt and ptt," *Photochemistry and Photobiology*, Vol. 96, pp. 219–231, 2020.

17. Dong, Z., K. Xue, A. Verma, J. Shi, Z. Wei, X. Xia, K. Wang, and X. Zhang, "Photothermal therapy: a novel potential treatment for prostate cancer," *Biomaterials Science*, Vol. 12, pp. 2480–2503, 2024.

18. Malekzadeh, R., T. Mortezazadeh, W. Abdulsahib, M. Hamblin, B. Mansoori, F. Alsaikhan, and B. Zeng, "Nanoarchitecture-based photothermal ablation of cancer: a systematic review," *Environmental Research*, p. 116526, 2023.

19. Hu, J.-J., Y.-J. Cheng, and X.-Z. Zhang, "Recent advances in nanomaterials for enhanced photothermal therapy of tumors," *Nanoscale*, Vol. 10, pp. 22657–22672, 2018.

20. Lv, S., Y. Miao, D. Liu, and F. Song, "Recent development of photothermal agents (ptas) based on small organic molecular dyes," *ChemBioChem*, Vol. 21, p. 2098, 2020.

21. Caldas, M., A. C. Santos, F. Veiga, R. Rebelo, R. L. Reis, and V. M. Correlo, "Melanin nanoparticles as a promising tool for biomedical applications- a review," *Acta Biomaterialia*, Vol. 105, pp. 26–43, 2020.

22. Tian, L., X. Li, H. Ji, Q. Yu, M. Yang, L. Guo, L. Huang, and W. Gao, "Melanin-like nanoparticles: advances in surface modification and tumour photothermal therapy," *Journal of Nanobiotechnology*, Vol. 20, p. 485, 2022.

23. Wang, X., J. Sheng, and M. Yang, "Melanin-based nanoparticles in biomedical applications: From molecular imaging to treatment of diseases," *Chinese Chemical Letters*, 2018.

24. Sun, J., Y. Han, J. Dong, S. Lv, and R. Zhang, "Melanin/melanin-like nanoparticles: As a naturally active platform for imaging-guided disease therapy," *Materials Today Bio*, Vol. 23, p. 100894, 2023.

25. Chinchulkar, S. A., P. Patra, D. Dehariya, A. Yu, and A. K. Rengan, "Polydopamine nanocomposites and their biomedical applications: A review," *Polymers for Advanced Technologies*, 2024.

26. Liu, Y., K. Ai, J. Liu, M. Deng, Y. He, and L. Lu, "Dopamine-melanin colloidal nanospheres: An efficient near-infrared photothermal therapeutic agent for in vivo cancer therapy," *Advanced Materials*, Vol. 25, no. 9, pp. 1353–1359, 2013.

27. Dong, Z., H. Gong, M. Gao, W. Zhu, X. Sun, L. Feng, and Z. Liu, "Polydopamine nanoparticles as a versatile molecular loading platform to enable imaging-guided cancer combination therapy," *Theranostics*, Vol. 6, no. 7, pp. 1031–1042, 2016.

28. Kang, S., R. Baskaran, B. Ozlu, E. Davaa, J. Kim, B. Shim, and S. Yang, "T1-positive mn^{2+}-doped multi-stimuli responsive poly(l-dopa) nanoparticles for photothermal and photodynamic combination cancer therapy," *Biomedicines*, Vol. 8, no. 10, p. 417, 2020.

29. Li, Y., X. Liu, W. Pan, N. Li, and T. B., "Photothermal therapy-induced immunogenic cell death based on natural melanin nanoparticles against breast cancer," *Chemical Communications*, 2020.

30. Kim, M. A., S. D. Yoon, J. S. Lee, and C.-M. Lee, "Melanin-peg nanoparticles as a photothermal agent for tumor therapy," *Materials Today Communications*, Vol. 25, p. 101575, 2020.

31. Jiang, Q., Z. Luo, Y. Men, P. Yang, H. Peng, R. Guo, and W. Yang, "Red blood cell membrane-camouflaged melanin nanoparticles for enhanced photothermal therapy," *Biomaterials*, Vol. 143, pp. 29–45, 2017.

32. Chen, A., J. Sun, S. Liu, L. Li, X. Peng, L. Ma, and R. Zhang, "Effect of metal ions on endogenous melanin nanoparticles for magnetic resonance imaging contrast agents," *Biomaterials Science*, 2019.

33. Seçkin, I., B. Kaleli, E. Sönmez, G. Kaleli Can, A. Özcan, B. Büyüksaraç, S. Avaz Seven, and E. Baysoy, "Coating of nitinol guidewire with manganese ion chelated natural melanin nanoparticles for mri," in *2024 Medical Technologies Congress (TIPTEKNO)*, (Mugla, Turkiye), pp. 1–4, 2024.

34. Baysoy, E., B. Ayan, G. Kaleli-Can, B. Büyüksaraç, and C. Liu, "Mri of a surgical guidewire in a hydrogel phantom: Effects of ferric ion chelated natural mnps," in *2023 Medical Technologies Congress (TIPTEKNO)*, (Famagusta, Cyprus), pp. 1–4, 2023.

35. Tai, S., Y. Sun, J. M. Squires, H. Zhang, W. K. Oh, C.-Z. Liang, and J. Huang, "Pc3 is a cell line characteristic of prostatic small cell carcinoma," *Prostate*, Vol. 71, no. 3, pp. 306–314, 2011.

36. Xu, Z., Z. Chen, W. Wang, X. Meng, X. Wang, Y. Xia, Q. Meng, Y. Li, R. Song, and G. Chen, "Cuttlefish ink-derived melanin nanoparticle-embedded tremella fuciformis polysaccharide hydrogels for the treatment of mrsa-infected diabetic wounds," *International Journal of Biological Macromolecules*, Vol. 277, p. 134342, 2024.

37. Regan, D., A. Mavridi-Printezi, L. Payne, M. Montalti, P. Borri, and W. Langbein, "Optical absorption and dichroism of single melanin nanoparticles," *The Analyst*, Vol. 148, no. 15, pp. 3531–3542, 2023.

38. Liang, Y., R. Li, H. Sun, J. Dan, Z. Su, Y. Kang, Q. Zhang, S. Shi, J. Wang, and W. Zhang, "Functionalized natural melanin nanoparticle mimics natural peroxidase for total antioxidant capacity determination," *Sensors and Actuators B: Chemical*, Vol. 359, p. 131541, 2022.

39. Xu, N., A. Hu, X. Pu, J. Li, X. Wang, J. Wang, Z. Huang, X. Liao, and G. Yin, "Fe(iii)-chelated polydopamine nanoparticles for synergistic tumor therapies of enhanced photothermal ablation and antitumor immune activation," *ACS Applied Materials & Interfaces*, Vol. 14, no. 14, pp. 15894–15910, 2022.

40. Tuchin, V., "Tissue optics and photonics: Light-tissue interaction," *Journal of Biomedical Photonics Engineering*, Vol. 1, pp. 98–134, 06 2015.

41. Mavridi-Printezi, A., A. Menichetti, D. Mordini, and M. Montalti, "Functionalization of and through melanin: Strategies and bio-applications," *International Journal of Molecular Sciences*, Vol. 24, no. 11, 2023.

42. Zou, Y., T. Wu, N. Li, X. Guo, and Y. Li, "Photothermal-enhanced synthetic melanin inks for near-infrared imaging," *Polymer*, Vol. 186, p. 122042, 2020.